Platinum Graphene Catalytic Condenser for Millisecond Programmable Metal Surfaces

Tzia Ming Onn[1,2], Sallye R. Gathmann[1,2], Silu Guo[2], Surya Pratap S. Solanki[1,3], Amber Walton[2], Benjamin J. Page[4], Geoffrey Rojas[5], Matthew Neurock[1,2], Lars C. Grabow[1,3], K. Andre Mkhoyan[2], Omar A. Abdelrahman[1,4], C. Daniel Frisbie[1,2], Paul J. Dauenhauer[1,2*]

[1] Center for Programmable Energy Catalysis (CPEC), University of Minnesota, 421 Washington Ave. SE, Minneapolis, MN, USA 55455.

[2] University of Minnesota, Department of Chemical Engineering & Materials Science, 421 Washington Ave. SE, Minneapolis, MN, USA 55455

[3] William A. Brookshire Department of Chemical and Biomolecular Engineering and Texas Center for Superconductivity (TcSUH), University of Houston, Houston, TX, USA, 77204

[4] Department of Chemical Engineering, University Massachusetts Amherst, 686 N. Pleasant Street, Amherst, MA, USA, 01003

[5] Characterization Facility, University of Minnesota, 100 Union Street SE, Minneapolis, MN, 55455, USA

* Corresponding author: hauer@umn.edu

Abstract. Accelerating catalytic chemistry and tuning surface reactions requires precise control of the electron density of metal atoms. In this work, nanoclusters of platinum were supported on a graphene sheet within a catalytic condenser device that facilitated electron or hole accumulation in the platinum active sites with negative or positive applied potential, respectively. The catalytic condenser was fabricated by depositing on top of a p-type Si wafer an amorphous HfO_2 dielectric (70 nm), on which was placed the active layer of 2-4 nm platinum nanoclusters on graphene. Potential of +/-6 V applied to the Pt/graphene layer relative to the silicon electrode moved electrons into or out of the active sites of Pt, attaining charge densities more than 1% of an electron or hole per surface Pt atom. At a level of charge condensation of +/-10% of an electron per surface atom, the binding energy of carbon monoxide to a Pt(111) surface was computed via density functional theory to change 24 kJ mol^{-1} (0.25 eV), which was consistent with the range of carbon monoxide binding energies determined from temperature programmed desorption (ΔBE_{CO} of 20±1 kJ mol^{-1} or 0.19 eV) and equilibrium surface coverage measurements (ΔBE_{CO} of 14±1 kJ mol^{-1} or 0.14 eV). Impedance spectroscopy indicated that Pt/graphene condensers with potentials oscillating at 3,000 Hz exhibited negligible loss in capacitance and charge accumulation, enabling programmable surface conditions at amplitudes and frequencies necessary to achieve catalytic resonance.

1.0 Introduction. Over the past century, metal surfaces have been synthesized for precise electronic interaction with adsorbates to accelerate reactions and control catalytic pathways.[1,2] Bulk metals were converted to nanoclusters supported on metal oxides and carbon surfaces, providing higher dispersion and increased densities of edge, step, and terrace sites.[3,4,5] These active metal surfaces were further refined by alloying with other metals[6,7], adding promoters and inhibitors that further modify their properties,[8,9] and by designing the catalyst/support interactions.[10,11] Precise synthesis of more advanced nanoparticles and surface design has included core-shell particles[12,13], intermetallic surfaces[14,15], and single atom alloys[16,17] to provide more electronic specification at the active site by altering the coordination of the atoms and the composition of nearest neighbors.[18] Such synthetic methods, however, require precise surface structures in stable conformations and only provide discrete options for active sites that are static on the time scale of the catalytic turnover.

An alternative approach to catalyst design directly tunes the electron density of the active site by stabilizing positive or negative charge in the exposed catalytic surface.[19,20] We have recently described the method of a 'catalytic condenser' that uses a high-*k* dielectric HfO_2 layer to separate a

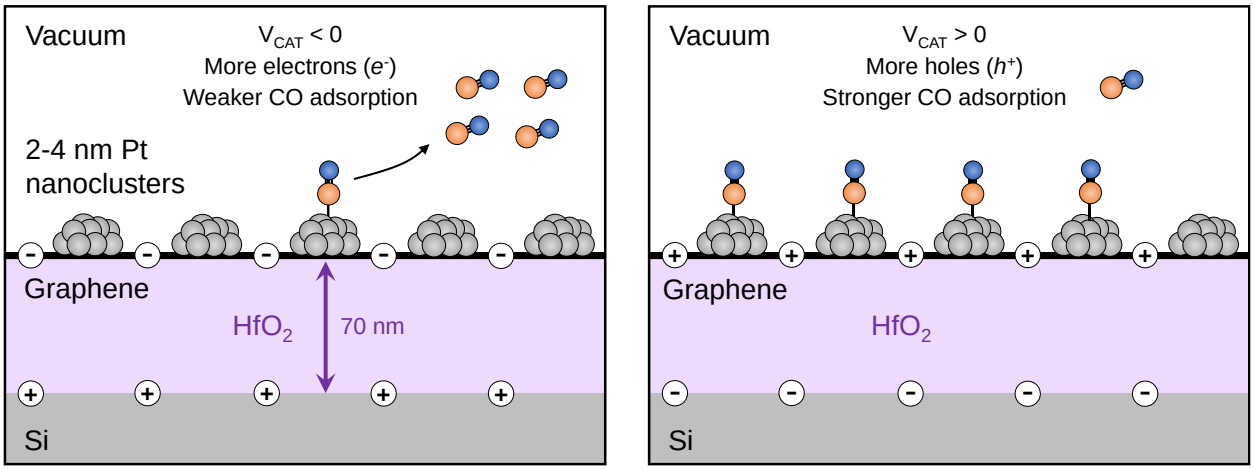

Scheme 1. Adsorption of carbon monoxide (blue oxygen, orange carbon) on the platinum-graphene active layer of a catalytic condenser with negative (left) and positive (right) charge condensation. Charge condensed in the active layer distributes between the graphene and a discontinuous layer of platinum nanoclusters that are 2-4 nm in height and alters the binding energy of carbon monoxide.

conductive silicon electrode from a conductive active layer of ultrathin amorphous alumina on graphene.[21] In this example, the amorphous alumina layer is a solid Lewis acid catalyst, while the supporting graphene rapidly distributes charge across the device surface. When a positive voltage bias is applied to the active alumina/graphene layer relative to the silicon electrode, the alumina catalyst active sites are depleted of electrons, making them more acidic and faster at dehydrating alcohols such as isopropyl alcohol.

Synthesizing the catalytic condenser stack design with a metal-on-graphene active layer (instead of an oxide on graphene) extends condenser applicability to many important metal-catalyzed chemistries. However, electronically biasing metals by stabilizing charge at the surface requires unique design of the metal layer. Metals have about an order of magnitude higher catalytic active site density than oxides such as alumina (10^{15} vs. 10^{14} sites cm^2, respectively)[22]; more charge per unit area must be stabilized to electronically perturb the catalytic active site. Additionally, electric fields that extend through the catalytic condenser from the electrode to the catalytic metal layer are more efficiently screened by metal layers than by oxide layers; the catalytic active sites must be close to the graphene layer stabilizing the electrode countercharge (i.e., a thin metal catalyst layer).

Platinum in particular is a useful catalyst due to its surface electron density that binds adsorbates sufficiently strongly to break hydrocarbon bonds and accelerate chemistry. Platinum is an efficient reforming catalyst of alkanes and oxygenates[23,24], a selective hydrogenation and dehydrogenation catalyst[25,26,27], and an active surface for oxygen reduction in fuel cells[28,29], among many other catalytic applications. Platinum is therefore a highly characterized catalytic material in many forms including single crystals surfaces[30,31], nanoclusters[32,33], alloys[34,35], and single atoms[36,37], making it an effective probe metal for modulation in a catalytic condenser.

In this work, the active layer of a HfO_2-based catalytic condenser was synthesized from platinum on graphene. As depicted in **Scheme 1**, platinum active sites were comprised of thin nanoclusters several atoms thick (~2-4 nm) dispersed on a continuous graphene sheet. Lower platinum loading decreased the total number of active sites and increased the charge stabilized per active site. The active layer of platinum on graphene was separated from a conductive p-type silicon substrate by 70 nm of insulating, amorphous HfO_2. Under negative bias ($V_{CAT} < 0$), electrons accumulating in the graphene and platinum reduced the binding energy of adsorbates such as carbon monoxide. Likewise, positive bias ($V_{CAT} > 0$) depleted electrons in the platinum and graphene and increased adsorbate binding energy. The physical and electronic characteristics of this platinum/graphene catalytic condenser were characterized to demonstrate a tunable metal surface with substantial variation in the electronic

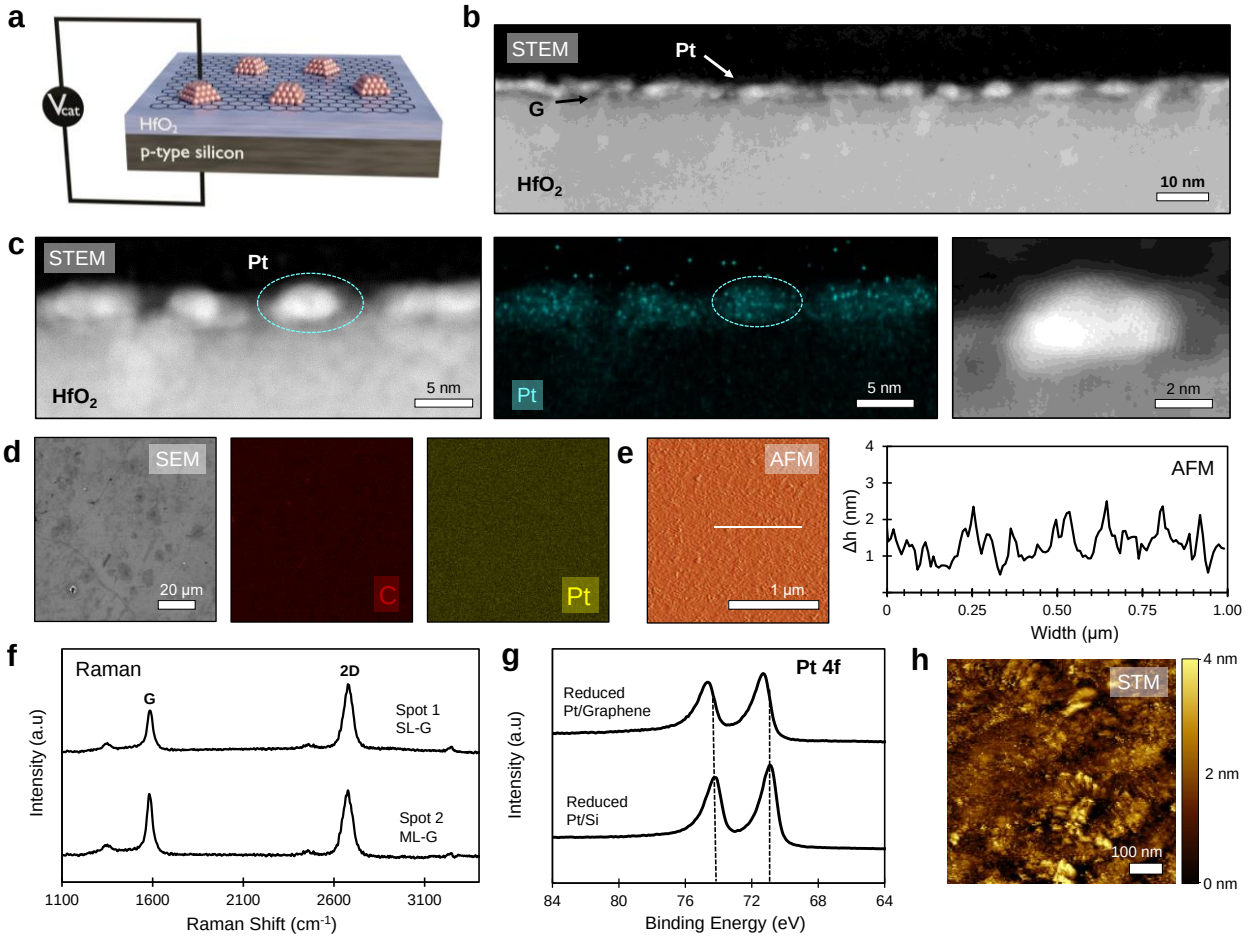

Figure 1. Platinum graphene catalytic condenser structure and composition. (a) Illustration of a Pt Graphene Catalytic Condenser device. **(b-c)** Cross-sectional TEM of the Pt/graphene active layer on HfO_2 insulating layer. The image of the device fibbed to a cross sectional width of ~30 nm indicates that the Pt nanoclusters are ~2-4 nm thick and separated by exposed graphene. The scale bars are shown in the respective TEM images. **(d)** Top-down SEM shows patches of multi-layer graphene with hexagonal domains and the EDS indicates uniform distribution and composition of carbon and platinum across the device. The scale bar is 20 µm. **(e)** AFM image (Scale bar of 1 µm) and height profile show minimal variation in active layer height across the device surface, consistent with the cross-section TEM. **(f)** Raman spectra of graphene collected at different spots on the device confirmed single layer (SL) and multilayer (ML) graphene on the device surface. **(g)** XPS Pt 4f spectra of the reduced Pt/G and reduced Pt/Si indicate a ΔBE of ~ 0.3 eV of Pt in the reduced Pt/G. **(h)** STM image of the Pt/G surface showing metal cluster morphologies and charged surfaces.

properties of active sites, even when oscillating applied potential bias at frequencies above 1,000 Hz.

2.0 Results and Discussion. The Pt/Graphene/HfO_2/Si catalytic condenser depicted in **Scheme 1** and **Figure 1a** was fabricated with full details described in the Methods Section and the Supporting Information. Beginning with a conductive p-type silicon wafer substrate (~1 cm^2), an electrically insulating HfO_2 layer was grown by atomic layer deposition (ALD) at 100 °C. The HfO_2 thickness, as measured by an ellipsometer, increased linearly with the number of ALD cycles, and the selected thickness of 70 nm was achieved in 500 cycles consistent with prior examples.[38,39] On top of the HfO_2 layer, a ca. 1 cm^2 graphene sheet was transferred using an established polymethyl methacrylate (PMMA)-based method to provide a conductive sheet across the insulating layer.[40,41] While a gold contact was added to earlier catalytic condenser devices[21], this was not included for the current device with the Pt/graphene active layer to avoid its participation in carbon monoxide

adsorption. Finally, Pt was deposited on graphene by electron beam evaporation of a pure Pt source and reduced in flowing H_2 at 150°C in a tube furnace for an hour.

The resulting catalytic condenser stack and active platinum/graphene layer were visible from the cross-sectional scanning transmission electron microscopy (STEM) image of **Figures 1b** and **1c**. On top of the amorphous HfO_2 insulating layer was a thin ~0.4 nm layer of graphene followed by an ultrathin Pt layer just a few nanometers thick, which appeared discontinuous. Focused-ion beam (FIB) cross-sectioning of the sample allowed for observation of individual particles of Pt between regions of exposed graphene; these particles were also distinguished using energy-dispersive X-ray (EDX) spectroscopy, as shown in **Figure 1c**. Individual Pt particles exhibited a high degree of crystallinity with the expected lattice structures for 2-4 nm nanoclusters (See **Figure S4**). From the plan view obtained by SEM as shown in **Figures 1d** and **S5**, the surface of the device comprised regions of single (light grey) and multi-layer (dark grey) graphene with several hexagonal-shaped domains visible and consistent with previous results.(21) The presence of these layers of graphene was confirmed by Raman spectra collected over 20 spot sites in **Figures 1f** and **S6**. More importantly, SEM-EDX verified that both carbon (C) and Pt were evenly distributed across the device surface (**Figure 1d**).

The catalytic condenser's surface roughness was then characterized by atomic force microscopy (AFM) as shown in **Figure 1e** and **Figure S7**. Over a two-by-two-micron region, variation in surface height (Δh) of the majority of the surface was only ~2 nm; the AFM tip was not capable of providing lateral resolution to observe individual particles. XPS measurements in **Figure 1g** showed a difference in binding energy for reduced Pt on graphene, with Pt $4f_{5/2}$ at 74.6 eV and Pt $4f_{7/2}$ at 71.3 eV when compared to reduced Pt on Si samples, with Pt $4f_{5/2}$ at 74.3 eV and Pt $4f_{7/2}$ at 70.9 eV. The 0.3 to 0.4 eV shift in binding energy has been attributed to enhanced interaction in the Pt-C due to the C π*–Pt d hybridization only observable in low loadings of Pt nanoparticles(42,43). This Pt-C interaction, detectable only after reduction, should allow for improved modulation of electron density of the Pt clusters. These observations, as well as height profiles obtained from the scanning tunneling microscopy (STM) image in **Figure 1h** and **Figure S8**, are consistent with a thin discontinuous layer of Pt nanoclusters 2-4 nm in height on a continuous layer of graphene.

The insulating amorphous HfO_2 layer functions to stabilize opposing charge between the condenser Si electrode and the platinum/graphene active layer, with the extent of charge condensation dependent on the thickness and quality of the HfO_2 film. We have previously characterized ALD-grown 70 nm HfO_2 films and determined that they remain amorphous at or below 350 ºC; XRD peaks associated with crystalline HfO_2 only appear when heated to 400 ºC or above.(21) The crystalline phase of HfO_2 exhibits a lower dielectric constant (~17 versus 26 for amorphous HfO_2), and the crystallized HfO_2 film is more likely to exhibit pinholes that conduct current between the active catalyst layer and the underlying electrode.(44,45,46,47,48) Operating the catalytic condenser at temperatures below 400 ºC allows for broad application of Pt active sites to many catalytic reactions while also achieving the highest amount of charge condensation at the active site.

Condenser Electronic Properties. The electronic properties of the Pt/graphene catalytic condenser were measured as shown in **Figure 2**. In **Figure 2a-2b**, the amount of charge stored in the active Pt graphene layer was determined from current-voltage (I-V) measurements of both a graphene condenser (without Pt) and the full Pt/graphene condenser, varying from -1.0 to +1.0 V at different sweep rates. Comparable results were obtained from I-V curves measured at larger sweep rates from -6.0 V to +6.0 V, **Figure S9**. The graphene device without Pt exhibited displacement current densities in the range of 10-50 nA cm^{-2}, linearly varying with the corresponding sweep rates and consistent with a graphene condenser capacitance of 35 nF cm^{-2}, as shown in **Figure 2b-2c**.(21) In stark contrast, the platinum/graphene condenser achieved current densities of ~500 nA cm^{-2}, a ten-fold increase over the graphene-only device capacitance to 350 nF cm^{-2}, when measured at room temperature. The added Pt nanoparticles dramatically increased the total capacitance of the condenser stack, which is consistent with either charge injection into the particles or their polarization.

The box-shaped displacement current-voltage measurements of **Figure 2a** indicate that electronic charge accumulated in both condensers with active

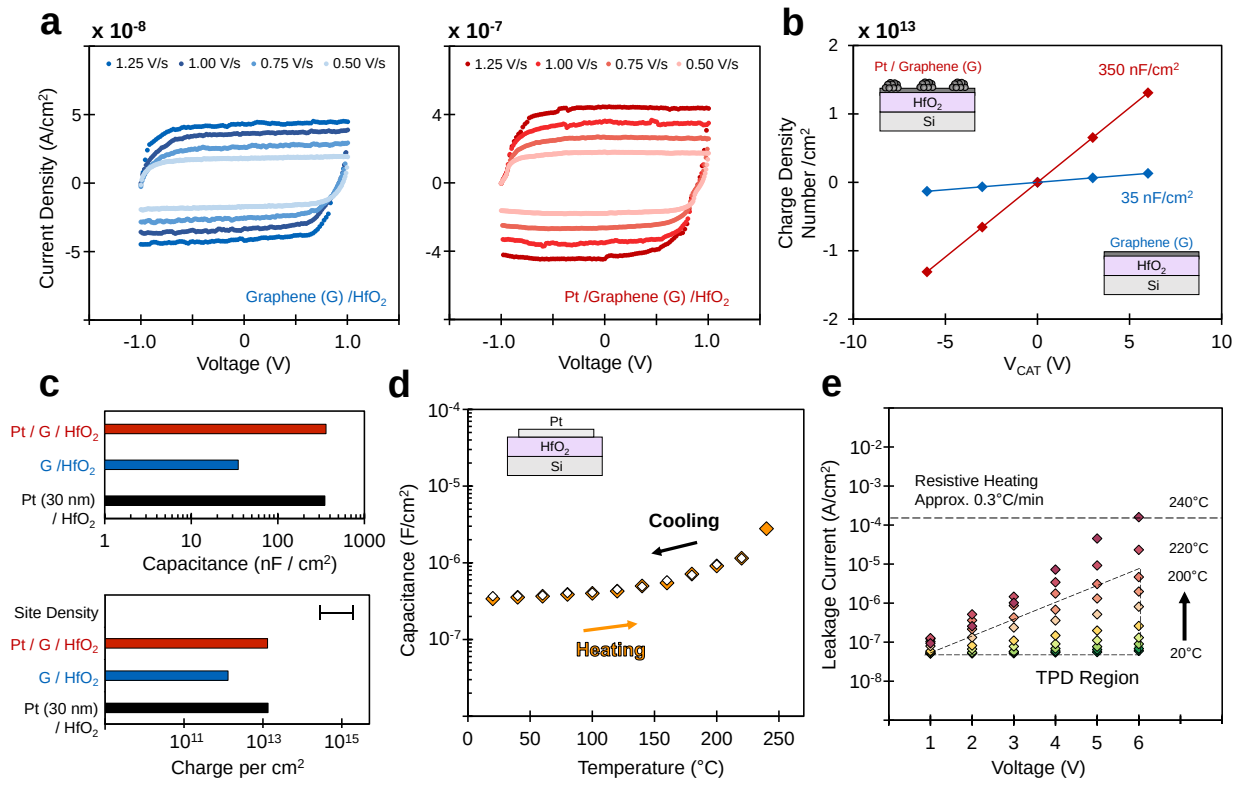

Figure 2. Electronic properties of the Pt /graphene catalytic condenser. (a) I-V curves of graphene on HfO_2 on Si (blue) and Pt/graphene on HfO_2 on Si (red). **(b)** Accumulated charge density measured by I-V curves (complete I-V curves in the Supporting Information) of both devices as a function of applied bias, V_{CAT}. **(c)** Device capacitance with Pt/graphene (red), graphene (blue), and Pt only (black). Charge accumulation at ± 6 V relative to the estimated Pt active site density range. **(d)** Measured device capacitance as a function of temperature. **(e)** Leakage current through the HfO_2 insulating layer as a function of temperature in A cm^{-2}.

layers of graphene (**blue, left**) and platinum/graphene (**red, right**). Based on the measured capacitance, the condenser with only graphene (no Pt) stabilized approximately 10^{12} (e^- or h^+) cm^{-2} for V_{CAT} of $\pm$6.0 V; for the same potential bias, charge condensation increased by an order of magnitude up to ~10^{13} (e^- or h^+) cm^{-2} when platinum was deposited on top of the graphene (**Figure 2b-2c**). The difference of these two electron densities indicates that charge is primarily accumulating in the Pt nanoclusters (holes or electrons at V_{CAT} greater or less than zero, respectively). Moreover, the 2-4 nm Pt/graphene device is condensing the maximum amount of charge for the applied potential and the thickness of the HfO_2 insulating layer. To demonstrate this, an alternative device (**Figure 2c**) comprised of a thick Pt layer (30 nm) on HfO_2 supported on Si also stabilized about ~10^{13} (e^- or h^+) cm^{-2}, which is the maximum achievable charge stabilized with the selected HfO_2 insulating film at room temperature.

The extent of charge accumulated in the Pt nanoclusters on graphene is sufficient to alter surface binding and adsorbate reactions. A continuous metal surface exhibits catalyst active site densities of ~10^{15} sites cm^{-2}. In the catalytic condenser, charge was accumulated in the amount of ~10^{13} (e^- or h^+) cm^{-2}, which would account for about 1% of an electron accumulated or depleted per surface Pt site on a continuous metal surface, assuming all charge accumulates at the surface. However, the deposited metal surface is discontinuous with regions of exposed graphene, possibly decreasing the number of surface sites, which could increase the charge accumulation/depletion beyond 1% of an electron per surface Pt atom. This is further complicated by the complexity of charge distribution in metal nanoclusters on crystalline planes; charges

accumulate near the Pt/graphene interface as well as highly undercoordinated Pt sites on the cluster surface. Consequently, the effect of charge accumulation on Pt was further assessed via calculations that examine model Pt clusters supported on graphene and the binding of adsorbates in the next section.

The temperature dependence of the condenser capacitance and leakage currents were measured over the working temperature range to assess the distribution of charge. As shown in **Figure 2d**, the device capacitance remained constant at ~340 nF cm^{-2} from room temperature up to 120 °C, after which it increased to ~980 nF cm^{-2} when heated to 240 °C, more than doubling the total amount of charge accumulated in the catalyst at room temperature. This increase in capacitance as the sample was heated was replicated within experimental error as the sample was cooled, indicating that capacitance is a reversible function of temperature for the HfO_2 insulating film. Condensers also exhibit leakage current, defined as the number of electrons that flow through the insulating HfO_2 layer with time. At room temperature, leak current was measured less than 0.1 $\mu A/cm^2$, as shown in **Figure 2e**. This leak current increased with increasing device temperature and applied voltage, as expected. At 240 °C and 6.0 V potential bias, the leakage current of the condenser device was on the order of microamps (μA) and below conditions that would lead to any significant resistive heating (ca. 0.3 °C increase min^{-1} at 100 μA) of the device (see supporting information for additional details).

Charge Distribution in Pt and Computed CO Binding Energy.* Our calculations via density functional theory (DFT) show that charge depletion or accumulation is more pronounced on metal surface sites. **Figure 3a** shows the charge variation on a cuboctahedral Pt nanocluster (ca. 2.7 nm) upon adding or removing electrons from the nanocluster. Even for a neutral nanocluster (V_{CAT} of 0 V), the surface is partially reduced, which in turn partially oxidizes atoms in the sub-surface layers. A similar result was reported by Holmberg et al. for a silver nanocluster comprising the same number of atoms as our Pt nanocluster.(49) Upon removing electrons (V_{CAT} > 0 V), the surface oxidizes whereas the electron density in the core remains essentially constant. Notably, the extent of oxidation is found to be highest for the most undercoordinated sites, i.e., corner atoms. Addition of electrons (V_{CAT} < 0 V) also follows a similar trend with maximum reduction at the surface, whereas the oxidation state of atoms beneath the surface remained unchanged. Interestingly, the charge was well-dispersed upon removal of electrons, while adding electrons resulted in more localized electrons on the corner atoms. This observation is further corroborated by the Bader charge distribution over all atoms shown in **Figure S32**.

CO adsorption on Pt is one of the widely studied metal-adsorbate interactions by DFT, but common generalized gradient approximation (GGA) functionals fail to capture the binding site preference for CO. Experimentally it has been observed that at low coverage CO selectively binds on the atop site on Pt(111), whereas standard GGA functionals predict preferential binding to three-fold sites. There have been many attempts to solve the so called 'CO/Pt(111) puzzle', but a generally valid solution remains elusive.(50,51,52) Moreover, CO is known to occupy bridge sites at intermediate coverages before returning to atop sites at near monolayer coverage. Based on DFT studies, Gunasooriya and Saeys attributed this shift in binding site to the negative surface charge of Pt atoms, which primarily destabilizes CO on atop sites by increasing the occupancy of the Pt-C σ* antibonding states.(53)

Figure 3b shows the variation in binding energy of CO on atop sites of different facets including Pt(111), Pt(100), Pt(122), and Pt(211) as function of surface charge over a much larger range than reported by Gunasooriya and Saeys. With increasing concentration of surface holes (h^+) CO binds more strongly; conversely, increased electron density on surface Pt atoms weakens CO binding, consistent with the trend observed by Gunasooriya and Saeys. With increasing surface coverage, repulsive adsorbate-adsorbate interactions weaken the binding energy of CO. We used the coverage-dependent binding energy model from Grabow et al. to show in **Figure S33** that the strength of these lateral interactions does not vary significantly with applied charge.(54)

Overall, DFT calculations predict a binding energy variation of about 0.25 eV (24 kJ mol^{-1}) for charge condensation in the range of +/- 0.10 e/surface Pt(111) atom, for a large range of coverages (see **Figure 3b** and **S33**). The center of the binding energy distribution, however, does

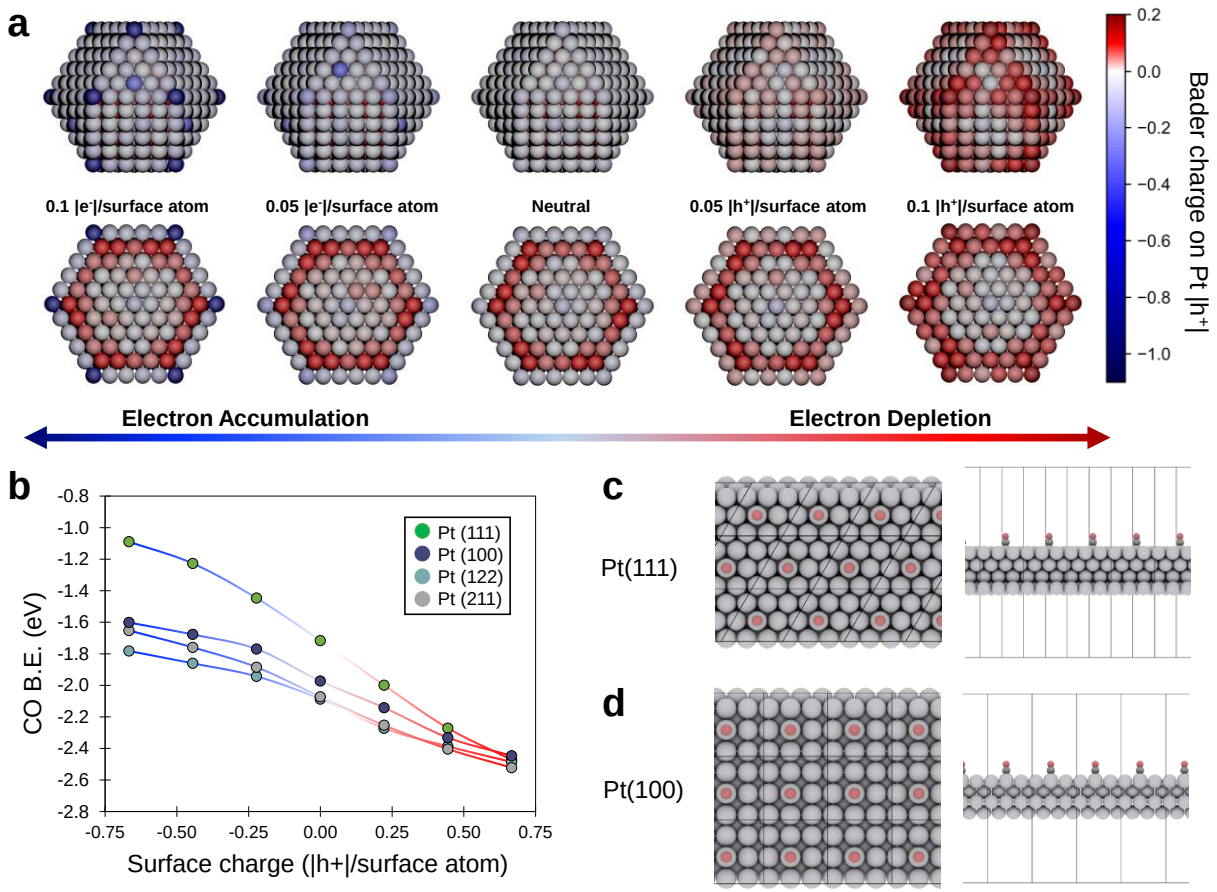

Figure 3. **(a)** Charge distribution in a nanoparticle with varying net charge. The lower panel is the top view of the slice at the middle of the particle. **(b)** Effect of surface charge on the CO* binding energy on different Pt facets considering only atop binding sites. **(c-d)** The top view and side view of the Pt(111) and Pt(100) unit cells; other facets are shown in the supporting information.

depend on the surface coverage and the selected DFT functional. For small variation in electron or hole accumulation (**Figure 3b**), variation of CO binding energy differs by Pt crystal plane (**Figure 3c, 3d**) with Pt(111), Pt(100), Pt(211), and Pt(122) exhibiting slopes of 120, 81, 80, and 71 kJ/mole-CO per electron/Pt-atom, respectively.

Temperature Programmed Desorption of Isotopic ^{13}C-Labeled Carbon Monoxide. Carbon monoxide strongly binds to Pt, making it an effective probe of the Pt surface. Depending on Pt surface structure (e.g., terrace, edge), oxidation state, exposed facet, and surface coverage ($0 < \theta_{CO} < 1$), the binding energy of CO on Pt has been reported to vary widely. On common Pt facets including (111) and (100), CO favors binding on atop sites.[50,55,56,57] The CO binding energy on Pt at low coverages has been reported in the range of ~125 to 160 kJ mol^{-1}, whereas the binding of CO at coverages greater than 50% decreases to as low as 50-100 kJ mol^{-1}.[22,58,56,57,59] Repulsive lateral interactions between neighboring CO* molecules limit loading to less than complete surface coverage.[22,57] The variation in binding energy of CO is detectable by temperature programmed desorption (TPD), with stronger binding species desorbing at higher temperatures.[60,61,62]

To evaluate the binding of carbon monoxide on the Pt/graphene catalytic condenser, the kinetics of gaseous ^{13}CO desorbing from the Pt/graphene condenser's surface was measured via TPD. The catalytic condenser (ca. 1.0 cm^2) was connected to two inert conductive wires providing voltage bias between the silicon substrate and platinum/graphene active layer. These wires suspended the condenser device in a heated quartz vacuum chamber connected to a dosing station, a vacuum pump system, and a quadrupole mass

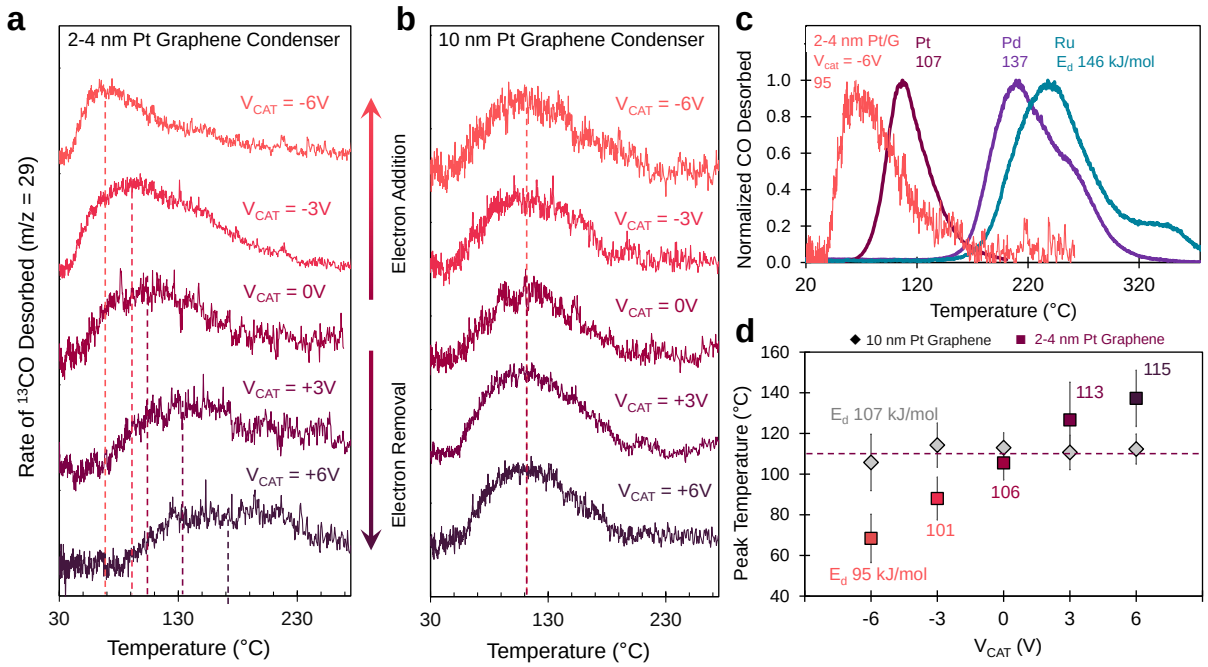

Figure 4. Temperature programmed desorption (TPD) of ^{13}CO on **(a)** 2 nm Pt and **(b)** 10 nm Pt on the graphene catalytic condenser with varying potential bias, V_{CAT}. **(c)** TPD of ^{13}CO on powdered samples of Pt, Pd, and Ru on alumina with the Pt/graphene condenser at V_{CAT} of -6V. **(d)** Peak maximum temperature of ^{13}CO desorption on Pt/graphene condensers with 2 nm (■) and 10 nm (◆) Pt layers with varying applied potential bias, V_{CAT}. Numbers associated with each potential are the estimated binding energy of ^{13}CO (E_d, kJ mol^{-1}) determined by the Redhead equation (Supporting Information). The dashed line represents the peak temperature of ^{13}CO desorption on powdered Pt on alumina.

spectrometer, QMS (**Figures S12-S15**). After the condenser was preheated to remove any surface adsorbates, reduced in-situ, and cooled, ^{13}CO was dosed at room temperature into the chamber to saturate the surfaces of the Pt nanoclusters. Starting from 20 ºC, the condenser was then heated to 400 ºC at a ramp rate of 10 ºC min^{-1} while the desorption of ^{13}CO was tracked by the QMS monitoring the mass-to-charge (m/z) of 29; isotopically-labeled ^{13}CO was selected to avoid m/z overlap with N_2 (which shares the same m/z of 28 with ^{12}CO), providing a clearer signal interpretation.

Temperature programmed desorption yielded a peak at m/z of 29 associated with ^{13}CO desorption from the Pt surface (**Figure 4a**). Control experiments (**Figure S19**) noted the absence of a m/z of 29 peak in the absence of a device, in the absence of dosing ^{13}CO, and in the case of ^{13}CO dosed to a graphene-only device (without Pt). Each trial was conducted with a fixed voltage bias during the entire temperature ramp. Without bias (V_{CAT} of 0 V), ^{13}CO was observed to desorb with a peak at 106±7 °C. Temperature programmed desorption of ^{13}CO on a supported Pt catalyst (5 wt % Pt/Al_2O_3, **Figure 4c** and **Figure S17)**, yielded a ^{13}CO desorption peak of 107 °C, consistent with peak desorption temperatures over the Pt/Graphene condenser (106 °C) in the absence of applied potential.

Comparison of the Pt/graphene condenser TPD peak with literature indicates general agreement, despite complications associated with different material structures and compositions, experimental conditions, and dosing conditions. For example, CO binds stronger on Pt(100) surfaces than on Pt(111)[58,56,57]. Another strong effect derives from dosing conditions and initial surface coverage of carbon monoxide on Pt. Carbon monoxide exhibits strong repulsive lateral surface interactions that reduce its binding energy, reducing the temperature of the CO desorption TPD peak by as much as ΔT_{peak} of 60 ºC for CO* surface coverages of 7 to 45% (~200 ºC to 140 ºC) on Pt(111)[57]. In contrast, TPD measurements in this work applied large doses of carbon monoxide, resulting in coverages that would exhibit lower CO

binding energies and peak desorption at lower temperatures, as observed in **Figure 4**.

Under negative potential bias applied to the Pt/graphene catalytic condenser, the desorption peak shifted to lower temperatures of 88±9 and 68±11 °C for V_{CAT} of -3V and -6V, respectively. Conversely, positive potential bias applied to the catalytic condenser shifted the ^{13}CO desorption peak to higher temperatures of 127±18 and 136±13 °C for V_{CAT} of +3V and +6V, respectively. Carbon monoxide was more weakly adsorbed to platinum when excess electrons accumulated near the binding site (V_{CAT} < 0 V), while electron depletion near the binding site strengthened the ^{13}CO binding energy (V_{CAT} > 0 V).

The shift in temperature associated with the ^{13}CO desorption peak maximum indicates that charge condensation within the 2-4 nm Pt/graphene catalytic condenser modulates the electronic state of the surface site(s) interacting with carbon monoxide. For a Pt/graphene condenser with a thicker 10 nm layer of Pt and an identical 70 nm HfO_2 insulating layer at the same potential biases, no detectable shift in ^{13}CO peak desorption temperature was observed (**Figure 4b**) at any of the considered voltages, -6V < V_{CAT} < +6V; all TPD profiles exhibited the same peak at ~109 °C despite changes in the sign (e.g., h^+ or e^-) or extent of applied potential bias. The results of peak temperature versus applied voltage are summarized in **Figure 4d** for thin (2-4 nm Pt) and thick (~10 nm Pt) catalytic condensers.

The absence of any shift in ^{13}CO TPD peak temperature in the 10 nm Pt/graphene condenser relative to the 2-4 nm device at variable potential bias, V_{CAT}, is probably due to the distribution of condensed charge in the Pt layer. The thicker 10 nm Pt layer likely shields the charge accumulating at the Pt/graphene interface from the Pt atoms and adsorbates at the surface, i.e., the voltage-induced charge is not accessible to the surface for the thicker Pt device. In contrast, the surface metal atoms in the 2-4 nm Pt/graphene condenser are closer to accumulating charge stabilized near the Pt/graphene interface; the induced charge likely distributes throughout the thinner Pt layer up to the surface where it can alter the binding of CO. Moreover, exposed graphene resulting from incomplete coverage of Pt (**Figure 1b-1c**) suggests that interfacial Pt sites close to the graphene surface experience a more significant charge perturbation.

Interpreting the binding energy of carbon monoxide on the 2-4 nm Pt/graphene catalytic condenser is complicated by the distribution of types of Pt sites, the heterogeneous accumulation of charge in Pt, and the lateral interactions of carbon monoxide on the Pt surface at different surface coverages. While the Pt/graphene condenser TPD peaks are broad over a wide temperature range, they are not significantly wider than the peaks of other metals from conventional powder catalyst samples including Pt, Pd, and Ru (all 5.0 wt.% on alumina, **Figure 4c**). Initial interpretation of the measured TPD peaks applied the Redhead model (assuming a desorption pre-exponential factor of 10^{13} s^{-1}, see supporting information for details), which indicated variation of the binding energy from about 95 to 115 kJ mol^{-1} between -6V and +6V, respectively (**Figure 4d**). While this initial analysis demonstrates a shift in binding energy, more complicated models accounting for multiple Pt sites, charge distribution, and lateral CO interactions are the focus of future work.

Infrared Spectroscopy and Isobars for CO Adsorption. The binding energy of carbon monoxide on the Pt/graphene condenser was also experimentally determined from adsorption isobars obtained via variable temperature infrared spectroscopy (VTIR).[63,64,65] The catalytic condenser was placed within a grazing incidence infrared spectroscopy cell (Harrick, Refractor Reactor) with the active surface of Pt/graphene exposed to the incident infrared light source (**Figure 5a**). Light reflecting from the condenser was directed to a HgCdTe detector and evaluated relative to a clean condenser surface background scan to identify absorption peaks associated with surface species on Pt or graphene. A fixed potential bias, V_{CAT}, was applied to the condenser by electrical feedthroughs through the top of the sample cell during each experimental trial at each temperature to collect an isobar profile. During each measurement, a fixed amount of pure carbon monoxide gas (30 mL min^{-1}) flowed continuously through the sample cell and over the condenser surface to maintain equilibrium between gaseous carbon monoxide and surface-adsorbed species.

A carbon monoxide adsorption isobar was collected by measuring the peak area at 2063 cm^{-1} (**Figure 5b-5c**) associated with CO* on Pt at fixed CO(g) partial pressure (1 atm), distinct from the two peaks at 2143 and 2269 cm^{-1} associated with

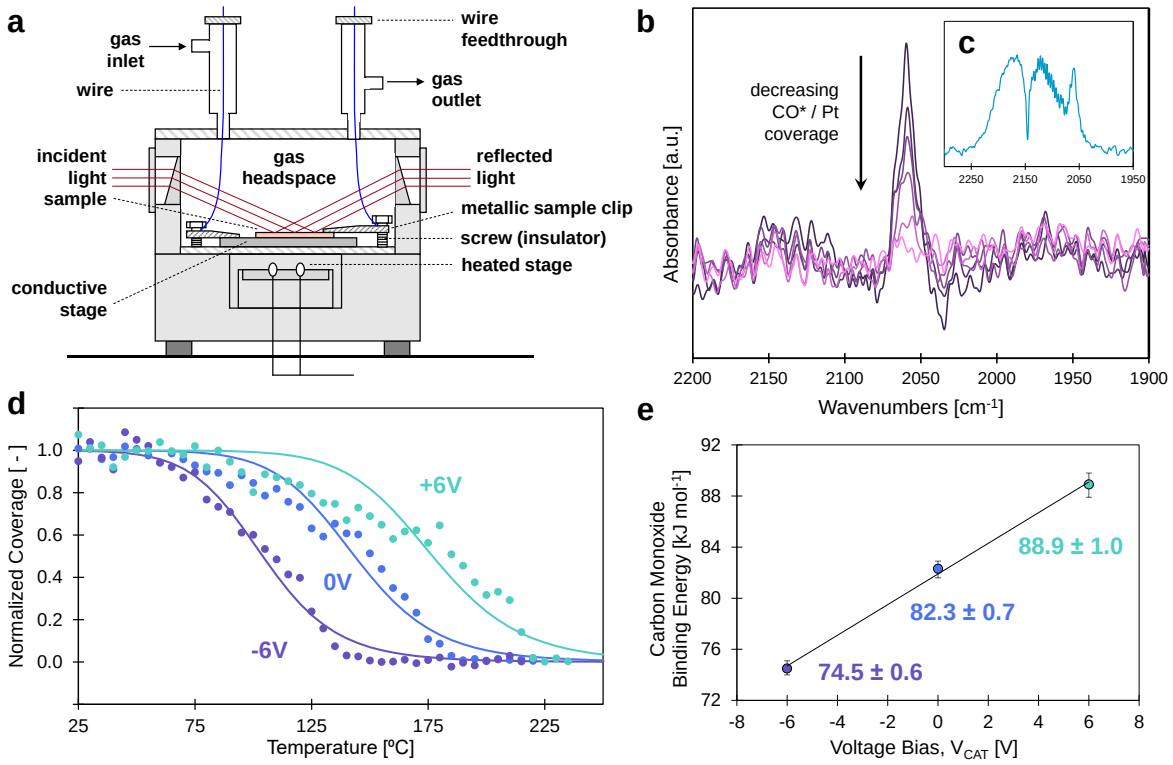

Figure 5. Infrared spectroscopy of CO on Pt/graphene condenser. (a) Grazing incidence sample cell with reflected light, heating stage, potential bias application, and continuous gas flow. **(b)** The absorbance peak at ~2063 cm^{-1} of CO on the Pt/graphene condenser subtracted from the background with varying surface coverage. **(c)** The absorbance spectrum containing two peaks at 2143 and 2269 cm^{-1} associated with gas-phase CO and a peak at 2063 cm^{-1} for adsorbed CO on the Pt/graphene condenser. **(d)** Adsorption isobars of the normalized CO coverage on the Pt/graphene condenser measured as a function of temperature for -6V (purple), 0V (blue), and +6V (teal). Points are experimental measurements, and lines are fitted Langmuir isobars. **(e)** The binding energy of ^{13}CO on the Pt/graphene condenser determined by fitting Langmuir isobars for -6, 0, and +6V potential bias.

gaseous CO vibrational modes.[66,67,68] The sample temperature (measured with a thermocouple within the sample cell) increased 3 K min^{-1}, which was sufficiently slow to ensure equilibrium between the flowing carbon monoxide gas and the platinum surface. CO adsorption isobars were acquired for potential biases, V_{CAT}, of -6, 0, and +6V between 20 to 225 ºC (**Figure 5d**). Isobars are normalized to the maximum area of the 2063 cm^{-1} peak at 20 ºC; the peak area decreased with increasing temperature consistent with reduced surface coverage of an exothermic CO adsorption on Pt.

From the isobar data shown in **Figure 5d**, it is apparent that positive bias applied to the Pt/graphene active layer relative to the condenser silicon electrode binds carbon monoxide more strongly, while negative bias weakens CO* binding energy. The platinum surface with negative bias (V_{CAT} of -6 V) exhibited lower CO* surface coverage at lower temperatures; the isobar with positive condenser potential bias exhibited the opposite trend. To quantify the shift in binding energy with applied potential bias, isobars were interpreted through Langmuir isotherms (see supporting information for details). Assuming that carbon monoxide becomes immobile upon adsorption onto the Pt/graphene condenser surface (ΔS_{ads} of 197 J mol^{-1} K^{-1}),[69] the heat of adsorption of carbon monoxide was determined to be -74.5±0.6, -82.3±0.7, and -88.9±1.0 kJ mol^{-1} for the potential bias, V_{CAT}, of -6, 0, and +6 V, respectively (**Figure 5e**). While absolute binding energy values derived from the adsorption isobars are lower than those from TPD, the trend of increasing CO binding energy with decreasing electron density in the Pt/graphene active layer is consistent across all measurements and DFT calculations.

Pt/Graphene Condenser Dynamics. Our results above demonstrate that the Pt/graphene catalytic condenser can statically shift the electronic properties of Pt active sites, but the next opportunity for applying this technology is the dynamic oscillation of active sites to accelerate and control catalytic reactions.[70,71] We have recently outlined a strategy for achieving significantly faster catalytic turnover frequencies, even beyond the Sabatier limit, by oscillating the energetic properties of catalyst sites.[72,73,74] Using the descriptor of the surface binding energy of a reaction intermediate, rate acceleration becomes substantial at an active site that is oscillating the binding energy of the selected intermediate in excess of ~0.2 eV (19.3 kJ mol^{-1}).[19,71] The Pt/graphene catalytic condenser described herein is now achieving binding energy variation of CO* near this limit (**Figures 4 & 5**).

The other requirement of a dynamic catalyst is sufficiently fast switching of the energetic state of the active site. For each catalyst composition (e.g., Pt, Pd) or electronic state (e.g., Pt, +3V), the rate limiting reactions of a more complex catalytic mechanism exhibit natural frequencies, defined as the inverse of the time constant of reaction (or adsorption/desorption, if that is rate limiting). When the active site oscillates at those natural frequencies, the rate accelerates beyond the Sabatier peak. For the considered model and real catalytic reactions, frequencies of interest occur in the range of 10 to 1,000 Hz.[19,75,76] With this frequency target, the Pt/graphene catalytic condensers were evaluated for their dynamic electronic characteristics.

During oscillation of the applied potential bias, V_{CAT}, to the catalytic condenser, charge moves laterally across the device a distance of ~1 cm in both the conductive silicon support and the Pt/graphene active layer. Each of these layers exhibits an electronic time constant associated with the resistivity of the layer, which can be compared to a condenser with a bare graphene surface (**Figure 6a**). The kinetics of lateral charge transfer across the bare graphene surface was then compared with the Pt/graphene device **Figure 6b**. Two other variations in device design were considered to achieve faster overall device speed: (i) inclusion of a gold star pattern (50 μm wide wires, centered on the graphene sheet) between the graphene and HfO_2 layers in **Figure 6c**, and (ii) inclusion of a highly conductive Pd layer between the Si and HfO_2 layers in **Figure 6d**.

Each independent layer was experimentally characterized by measuring the electrical resistance across the ~1 cm device by the method depicted in the inset of **Figure 6e**. By connecting two electrodes to each end of the layer of interest and measuring the current, the electrical resistance was determined for layers of silicon, graphene, palladium gold, and a star pattern of gold on graphene (**Au*/G**). From this resistance, a theoretical RC time constant, τ, was calculated for each of the five considered materials as the product of the measured resistance (R) and the device capacitance (C),

$$\tau = RC \qquad \text{(Eq. 1)}$$

The cutoff frequency was then calculated as the inverse of the RC time constant; additional details are provided in the supporting information. The selected silicon wafer, though conductive, was slow with a maximum achievable frequency of ~1 Hz over a distance of 1.0 cm. Graphene was substantially faster at ~1,600 Hz, which was accelerated to ~4,200 Hz when the gold star pattern was added. Finally, both palladium and gold exhibited frequencies in the range of 10^5-10^6 Hz, as expected of highly conductive metals.

The complete catalytic condenser was electronically characterized under dynamic conditions by an impedance spectrometer (**Figure 6f**). Similar to the electronic measurements performed on the condenser devices, two pin probes were used, one placed on the Pt/graphene layer and the other on the counter electrode, which was either the Si or Pd electrode that was made via shadow-mask patterned e-beam evaporation of a Pd source. Impedance spectra were then collected via application of a 2 V sinusoidal potential from 10 Hz to 10 MHz. The original design of Pt/graphene/HfO_2/Si with 70 nm of HfO_2 and 2-4 nm of Pt on graphene (**Figure 6b**) exhibited the expected ~350 nF/cm^2 capacitance when measured at low frequency (<100 Hz). However, capacitance significantly decreased below 1 nF/cm^2 as the frequency increased to 1,000 Hz. Similarly, the condenser containing only graphene (no Pt) exhibited the expected ~35 nF/cm^2 capacitance at

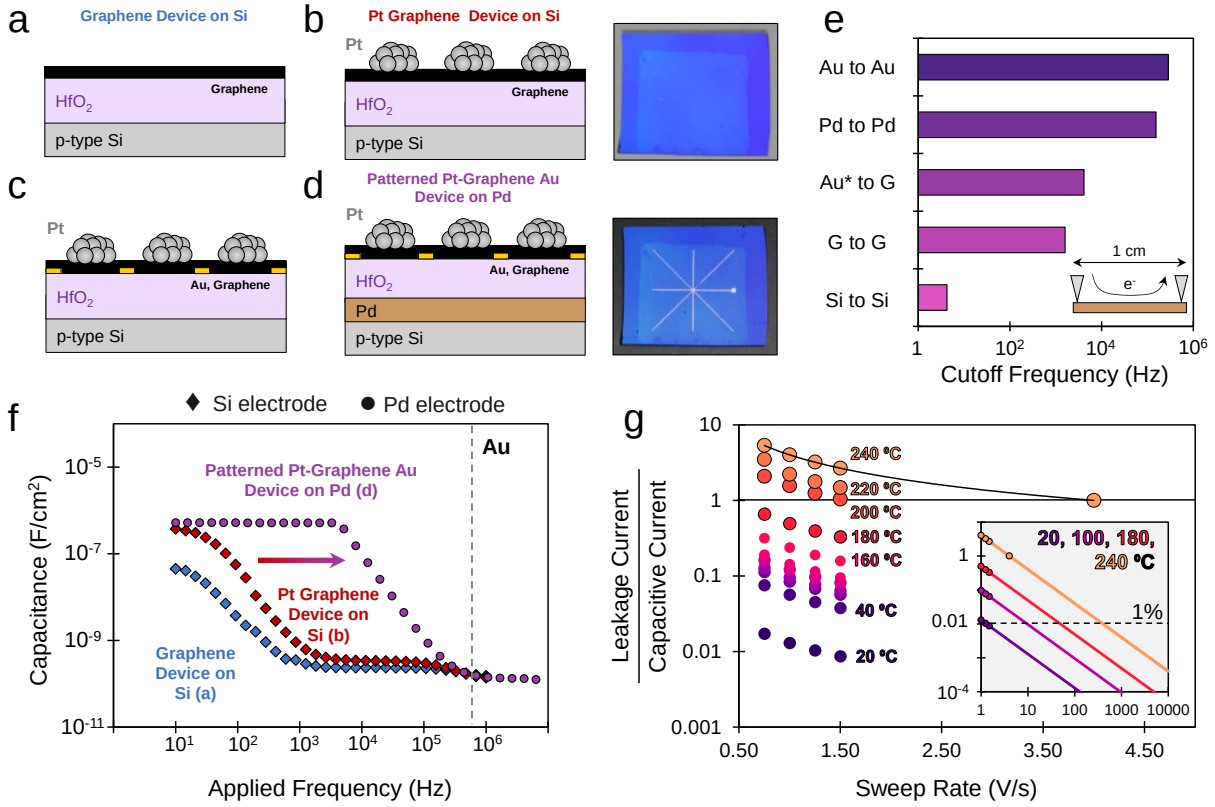

Figure 6. Dynamic Behavior of Pt/Graphene Catalytic Condenser. Catalytic condensers fabricated with: **(a)** Graphene on HfO_2 on Si, **(b)** Pt on graphene on HfO_2 on Si with accompanying photograph, **(c)** Pt on graphene on Au star pattern on HfO_2 on Si, and **(d)** Pt on graphene on Au star pattern on HfO_2 on Pd on Si with accompanying photograph. **(e)** The cutoff current frequency of a 1.0 cm material determined from measured conductivity; see supporting information for more details. **(f)** Capacitance of condenser devices as a function of applied frequency. **(g)** The measured (points) and predicted (lines) ratio of leakage current through the condenser relative to current capacitive current accumulating in the active layer as a function of oscillation frequency (proportional to voltage sweep rate) and device temperature.

low frequencies, before also decreasing in capacitance below 1 nF/cm^2 at 1,000 Hz.

The decrease in capacitance of the Pt/graphene condenser with increasing frequency was attributed to the relatively large resistivity of the lightly-doped silicon wafer which prevented uniform charge distribution over 1 cm^2 areas at timescales shorter than ~1 s. As shown in **Figure 6e**, the silicon sample achieves a cutoff conductive frequency of about 1 Hz for a 1 cm^2 wafer for the considered device capacitance. This limitation was evaluated by considering three alternative condenser designs: one with a gold active layer in place of Pt/graphene (not depicted), a second device with gold metal on either side of the HfO_2 (not depicted), and a third device with palladium between the silicon wafer and the HfO_2 insulating film (**Figure 6d**). Pd was selected for its conductivity and demonstrated HfO_2 growth on Pd surfaces, but any conductive metal should equivalently perform in terms of charge conductivity. The device with gold/HfO_2/Si also exhibited a decrease in capacitance beyond 10 Hz, consistent with Si limiting the overall lateral electron transport. In contrast, the device with gold on either side of the HfO_2 insulating film layer achieved high capacitance up to the megahertz frequency range (see supporting information), indicating that the limitation exists within the selected Si support. Finally, the device containing the additional internal layer of Pd (Pt/graphene/HfO_2/Pd/Si) exhibited high capacitance up to ~3,000 Hz, indicating that the increase in conductivity in the bottom electrode

when switching from Si to Pd shifted the overall device charge transport limitation to the active layer of Pt/graphene. Alternatively, high electrode conductivity could be achieved with a highly doped Si wafer. With this new design element, a fast conductive electrode, catalytic condensers can operate at high capacitance at speeds up to and beyond the range of interest for catalytic resonance.

Another key issue for dynamic operation of the catalytic condenser is the distribution of capacitive charge for active site perturbation and the charge lost to leakage current. While the leakage current measured in **Figure 2e** was low for all relevant conditions at static application, dynamically varying the potential can alter the ratio of capacitive current versus leakage current (i.e., current that accumulates charge in the active layer versus current that passes through the HfO_2 insulating layer). To measure the behavior of electrons with respect to these two different directions, Pt/graphene condensers were electronically measured at different temperatures with varying voltage sweep rates using the same probe system in **Figure S10** and methods described in the Supporting Information.

By these methods, the ratio of the leakage current to the capacitive current that leads to accumulated charge in the active layer is depicted in **Figure 6g** for voltage sweep rates of 0.75, 1.00, 1.25, 1.50, and 4.00 V s^{-1}. Below 200 ºC, all devices exhibit a majority of the current contributing to the accumulated charge in the active layer (capacitive current). As the temperature increases, leak current increases and more charge is lost to leakage between the Pt/graphene and Si wafer electrode. However, as the sweep rate increases (i.e., the applied oscillation frequency increases), the amount of current lost to leakage current decreases. For a device at 240 ºC, the applied current contributes equally to the active layer at a sweep rate of 4.00 V s^{-1}, above which most current contributes to accumulated charge in the catalytic active layer. For most considered oscillations of the Pt/graphene condenser, this corresponds to a frequency of about ~1 Hz.

Projecting the distribution of charge between capacitive and leakage current out to the frequencies of interest indicates that leakage should become negligible for dynamic operation of catalytic condensers. The measured data of **Figure 6g** were fit to an inverse power law and extrapolated to the frequency ranges of interest (inset, 10 to 10,000 V s^{-1}). As shown, a Pt/graphene catalytic condenser at room temperature operating at 100 V s^{-1} should lose only 0.01% of electrons to leakage current. At higher temperature of 240 ºC, less than 1% of electrons should be lost to leakage once the device operates above ~400 V s^{-1}, with even better device efficiency occurring at higher potential sweep rates. In the frequency region of interest for dynamic and programmable catalysts, most of the voltage applied to the device should result in active site perturbation with only negligible electrons lost to leakage.

The Metal Catalytic Condenser. The variation in carbon monoxide binding energy predicted by density functional theory on the platinum/graphene catalytic condenser is consistent with the experiments of carbon monoxide infrared spectroscopy and temperature programmed desorption. Most importantly, both experiments and computation indicate that depletion of electrons at the active site strengthens CO binding on Pt, while the addition of electrons weakens CO binding energy. More quantitatively, DFT calculations predicted that an electronic accumulation of -0.10 to +0.10 $|e^-|$ per surface atom will shift the CO* binding energy by about 24 kJ mol^{-1} (0.25 eV). Comparing this prediction to experiment is challenged by quantification of charge over the Pt surface; experiments measured the accumulation of ~10^{13} e-/cm^2 for V_{CAT} of +/- 6V, but the density of surface sites on a Pt film is up to ~10^{15} sites/cm^2 ($\geq$1% of an electron per surface site). In comparison, the TPD experiments of **Figure 4** measured a ΔBE_{CO} of ~20 kJ mol^{-1} for this degree of charge accumulation (~10^{13} e^-/cm^2, +/-6V). Similarly, the measured isobars of **Figure 5** were interpreted to result in ΔBE_{CO} of ~14 kJ mol^{-1} for the same +/- 6V bias. Both of these experimental measurements are larger than predicted by computation if only +/- 0.01 $|e^-|$ accumulates per active site. This could indicate that the Pt/graphene condenser has fewer than 10^{15} sites/cm^2 or that electrons are unevenly distributed in the Pt surface as depicted in **Figure 3a**, among other potential inaccuracies in calculation or interpretation of experimental data.

Enhancing the Pt/graphene catalytic condenser for stronger shifts in adsorbate binding energy will require accumulating more charge in fewer surface Pt atoms. Platinum can be deposited in smaller

clusters with higher dispersion, even down to single Pt atoms on graphene,[77,78]. These new Pt particles can also be designed to deliberately enhance active sites (i.e., edges, corners), with catalyst particle shapes, alloys, or core-shell structures that deliberately push accumulated charge to the surface. Additionally, more charge can be accumulated in the active layer with thinner dielectric films and materials with higher dielectric constants. For example, oxide ferroelectric films such as $BaTiO_3$ or $SrTiO_3$ exhibit dielectric constants significantly larger than HfO_2, providing capability to stabilize one-to-two orders of magnitude more charge in catalyst layers at the same applied potential.[79,80]

Electronically perturbing adsorbates on metals provides a new opportunity for tuning the energy profile of a catalytic cycle to enhance surface chemistry. As a platform technology, the catalytic condenser is a general approach for active site design that can tune the electronic state of both metals and metal oxides.[21] Instead of controlling the energies of surface species and transition states through active site design alone, a continuum of surface electronic states are accessible on a catalytic condenser via applied voltage, V_{CAT}, that were previously not available in the discrete atomic structure of surfaces. Catalysts can be optimized by selection of a specific applied potential that optimizes rate, selectivity, or active site stability.

The more advanced application of the catalytic condenser oscillates the binding energy of reacting surface species at the speed of the catalytic turnover.[72] By 'programming' the applied potential, V_{CAT}, to change with time as the surface reaction proceeds, the catalyst active site can provide optimal conditions for each elementary step independently. Simulation of a dynamic active site has predicted significant catalytic rate acceleration, even beyond the Sabatier peak, at 'resonance' oscillation frequencies that match natural frequencies of the rate limiting steps within a catalytic cycle.[72,73] These resonance frequencies have been predicted to occur above ~10-100 Hz, with variation of the onset of catalytic resonance depending on the selected combination of chemistry, active site, and reaction conditions (e.g., temperature) that determine elementary step kinetics.[19,75,76] The frequencies required for catalytic resonance are achievable with the Pt/graphene device; as shown in **Figure 6e**, the conductivity of electrons in the Pt/graphene layer is sufficiently high to operate at 100-1,000 Hz. When integrated into a catalytic condenser with a high conductivity electrode (e.g., a highly conductive metal), the entire device shuttles electrons into and out of the active layer sufficiently fast (10^2-10^3 Hz) to maintain high capacitance at the frequencies required for catalytic resonance (**Figure 6f**). With the capability to modulate the energy of adsorbates at frequencies above 100 Hz, the catalytic condenser has achieved the performance characteristics necessary to implement programmable catalysis for a host of metal-promoted surface reactions.

3.0 Conclusions. A catalytic condenser comprised of platinum nanoclusters on graphene was fabricated, characterized, and evaluated for its ability to modulate the binding energy of carbon monoxide with varying applied potential. The device consisted of 70 nm of an amorphous HfO_2 electrical insulating layer grown on conductive silicon; graphene was then transferred on top of HfO_2, and Pt was deposited onto the graphene by electron beam deposition. Electron microscopy, x-ray photoelectron spectroscopy, and atomic force microscopy indicated a continuous graphene film with a thin layer of independent Pt nanoclusters ~2-4 nm thick between regions of exposed graphene. The active layer of Pt/graphene accumulated ~10^{13} e^-/cm^2 with +/-6 V of potential bias, with most of the charge residing in the Pt cluster to achieve charge densities above 1% of an electron or hole per Pt active site. Density functional theory calculations indicated that charge accumulated in the particle distributed unevenly, with much of the charge residing near the particle surface. For carbon monoxide binding on atop sites, calculations predicted that accumulated charge of +/-0.10 e^-/surface-Pt-atom altered the binding energy by ~0.25 eV. Carbon monoxide binding was experimentally evaluated by the method of temperature programmed desorption. The Pt/graphene condenser with ~2-4 nm of Pt exhibited a peak in ^{13}CO desorption at 107 ºC, but the peak temperature shifted to lower and higher temperatures of 68 and 137 ºC with applied potential bias of -6V and +6V, respectively. Over this potential range, shifts in peak temperature associated with ^{13}CO desorption were interpreted as a change in carbon monoxide binding energy of 95

to 115 kJ mol^{-1}; positive bias increased the binding energy of CO* resulting in higher desorption temperatures. Equilibrium adsorption of carbon monoxide on the Pt/graphene condenser was also evaluated by grazing incidence infrared spectroscopy, resulting in adsorption isobars at temperatures of 20-240 ºC and fixed bias potentials of -6, 0, and +6V. By fitting a Langmuir isotherm over this potential range, the CO binding energy was estimated to shift from 74 (at V_{CAT} of -6 V) to 89 kJ mol^{-1} (+6 V). Experimental measurements of CO binding energy variation were consistent with computation, with positive potential bias applied to the active Pt/graphene layer resulting in stronger chemisorption. Finally, impedance spectroscopy determined that the Pt/graphene active layer could operate at ~10^3 Hz without a loss in capacitance, achieving fast conditions with significant shift in binding energy required for resonance programmable catalytic applications.

4.0 Methods. The platinum/graphene catalytic condenser was fabricated, verified by electron microscopy, atomic force microscopy, scanning tunneling microscopy, and spectroscopy, and evaluated by experimental catalytic reaction and computation. Complete research methods are described in the Supporting Information.

Catalytic Condenser Fabrication. Catalytic condensers were fabricated on a conductive p-type Si substrate (WaferPro) with sequential deposition of HfO_2, graphene, and Pt layer followed by a reduction in H_2. 70 nm of HfO_2 was grown from 500 HfO_2 ALD cycles at 100 °C in a flow-type ALD reactor (Kurt J Lesker ALD-150 LE). Each HfO_2 ALD cycle comprised of alternating exposures to the precursor, Tetrakis (dimethylamido) hafnium (TDMAH, t = 13 ms), and H_2O (t = 200 ms) with purges in between each step. Graphene on a Cu foil substrate, obtained commercially from Graphene Supermarket, was transferred on top of the HfO_2 layer using an existing PMMA-based method and retained electrical conductivity (**Figure S2**). A Pt layer (2 nm) was then grown on the graphene by e-beam evaporation of a pure Pt source. Each device was used to collect a full set of voltage modulated experimental reaction trials. Full descriptions of the fabrication process are available in the Supporting Information.

STEM, SEM, and EDX Analyses. The electron transparent cross-section of the devices for the STEM studies were prepared using Focused Ion Beam (FEI Helios NanoLab G4 dual beam). A preliminary amorphous Carbon (am-C) protection layer (~50 nm) was deposited on top of the sample using a sputter coater. Two additional protection layers of am-C (2 μm) and Pt (2 μm) were deposited on the region of interest. FIB ion beam was operated at 30 kV with 2 kV electron beam. STEM experiments were carried out on an aberration-corrected FEI Titan G2 60–300(S)TEM microscope equipped with a CEOS DCOR probe corrector, monochromator, and a super-X energy dispersive X-ray (EDX) spectrometer. HAADF-STEM images were obtained at 200 kV with 150 pA probe current. Camera length was 130 mm with probe convergence angle of 25.5 mrad. The detector inner and outer collection angles were set to be 55 and 200 mrad respectively. STEM-EDX elemental maps were obtained and analyzed via Bruker Esprit. SEM images and SEM-EDX maps were acquired using JEOL 6500 FEG-SEM. SEM images and SEM-EDX elemental maps were acquired under 5 kV. The SEM-EDX maps were quantified using the Aztec EDX analytical system (Oxford Instruments). For more details and results, refer to the Supporting Information.

Spectroscopy. Raman spectra of the condenser devices were collected using a Witec Alpha 300R confocal Raman microscope equipped with a UHTS300 spectrometer and a DV401 CCD detector. XPS spectra collection was performed on a PHI Versa Probe III XPS system (ULVAC-PHI) using a mono-chromated Al Kα X-ray source (1486.6 eV). The measurements were conducted using an X-ray spot size of 0.1 × 0.1 mm^2 with a power of 25 W under 15 kV. The survey spectra were measured using 280 eV pass energy and 1.0 eV/step. The data was processed with the Multipak software. Infrared spectra of the condenser devices exposed to CO was collected using a Thermo Scientific Nicolet iS50 FT-IR with a Mercury-Cadmium-Telluride (MCT) detector and a tailored Refractor Reactor Grazing Angle setup (Harrick Scientific). The incident angle is fixed at 75° and the window is a wedged ZnSe. To measure the effects of temperature with IR, the background is first collected at every experimental temperature. Pure CO is flowed into the sample chamber at 30 sccm and the IR spectrum is then collected and

subtracted. Full details on collections and analyses are available in the Supporting Information.

Temperature-Programmed Desorption. ^{13}CO TPD was carried out in a customized ultrahigh vacuum chamber. Isotopic ^{13}CO was selected as a probe molecule with a mass-charge ratio of 29. The fragment was monitored during the temperature ramp of the device, while potential bias was applied to the catalytic condenser. Full description of the equipment setup, device handling, temperature calibration, and the full TPSR process can be found in the Supporting Information.

Atomic Force Microscopy and Scanning Tunneling Microscopy. AFM profiles were measured by a Bruker Dimension Icon closed-loop atomic force microscope using the force-modulation technique with a force feedback setpoint of 581 pN. Probes were standard Si cantilevers calibrated before measurement with a spring constant of 0.674 N m^{-1}. STM measurements were performed using an Omicron low-temperature scanning tunneling microscope at room temperature under a vacuum of 8.0×10^{-10} mBar using a Pt/Ir probe. Samples were grounded through the Pt/graphene film. Differential spectra were collected from a Stanford Research Systems lock-in amplifier with a modulation signal of V_{mod} = 10 mV and f_{mod} = 10 kHz. Data were processed using the WSxM software.

Device Electronic Characterization. Capacitance measurements were collected from a probe station equipped with a source meter (Keithley 2611B and Keithley Test Script Builder). Conductive metal probes were carefully placed on the surface of the sample for the electrical measurements. Different voltage sweep-rates (1.50 V/s, 1.25 V/s, 1.00 V/s, 0.75 V/s, 0.50 V/s) were used to collect the I-V curves. For temperature-based experiments, a conductive sample stage was placed on top of a ceramic non-conductive hot plate. Probes were carefully placed on the sample's surface and on the conductive stage to measure capacitance and leakage current. The impedance spectra of the devices were recorded in a two-electrode configuration, like the setup used in capacitance measurement as described above. These measurements were performed with a Newtons PSM3750 multimeter equipped with an Impedance Analysis Interface 2 from the frequency range of 10 Hz to 10 MHz.

Computation. All periodic DFT calculations were performed using the Vienna ab initio simulation package (VASP)[81,82,83,84] employing a plane wave basis set under the Kohn-Sham formulation[85,86] along with the Atomic Simulation Environment (ASE)[87] for workflow management, visualization, and post-analysis. The electron exchange-correlation energy was determined within the generalized gradient approximation[88] using the PBE functional.[88.89] The projector augmented wave (PAW) method was used to describe the interaction between ion cores and electrons.[81,90] The valence electron wavefunction was expanded into a plane wave basis set with an energy cut-off of 400 eV, and spin polarization was enabled.

Geometry optimization calculations were performed using Gaussian smearing with a width of k_BT = 0.1 eV and subsequently extrapolated to 0 K. The self-consistent-field (SCF) cycle was stopped when the electronic energies were converged to 10^{-6} eV. Ionic relaxations were performed until the atomic forces were less than 0.02 eV/Å. The Brillouin zone was sampled with the Monkhorst–Pack scheme, using 16 × 16 × 16 k-points for bulk Pt lattice optimization, 4×4×1 for Pt surface calculations and Γ-point only for nanoparticle calculations. Bader charge analysis was performed to estimate partial electronic charges on the atoms.[91,92,93]

Gas-phase energies were computed using the already mentioned parameters except for a narrower Gaussian smearing width of 0.01 eV and ionic relaxations were performed until the atomic forces were less than 0.005 eV/Å. Additionally the dipole corrections were applied in all three cartesian directions keeping the gas molecule at a central position in a cell of size 15 Å × 15 Å × 15 Å. We define the adsorption energy as:

$$\Delta E = E_{act/ads} - E_{act} - E_{ads} \qquad \text{(Eq. 2)}$$

$E_{act/ads}$ is the total energy of the surface with adsorbate, E_{act} is the energy of optimized structure for the surface, and E_{ads} is the energy of isolated adsorbate molecule. In our definition, favorable binding is indicated by negative values of ΔE. All the optimized geometry and INCAR files are provided in the supplementary information.

The cuboctahedra platinum cluster comprising of 561 atoms was constructed using the optimized Pt bulk lattice constant of 3.968 Å. All the atoms were fixed to their bulk position and the Bader charges were calculated for this fixed geometry with applying dipole corrections in all directions.

All Pt surfaces i.e., Pt(111), Pt(100), Pt(211), and Pt(122) are represented by periodically repeated slabs separated by 30 Å of vacuum. For neutral systems, a dipole correction normal to the surface was applied. The charged calculations were performed by controlling number of electrons in the system by varying the NELECT parameter combined with the implementation of implicit solvation using VASPsol and without further dipole correction.[94,95] The dielectric constant used to screen the electrostatic potential in the vacuum space was set to 80, representative of water. We confirmed that the implicit solvation model had no effect on the CO binding energy of the neutral system.

Acknowledgements. We acknowledge financial support from the U.S. Department of Energy, Basic Energy Sciences Catalysis program (DE-SC0021163) and the Center for Programmable Energy Catalysis (CPEC), a Department of Energy, EFRC Energy Frontier Research Center. S.R.G. was supported by a Graduate Research Fellowship under Grant CON-75851, project 00074041. This research used resources of the National Energy Research Scientific Computing Center (NERSC), a U.S. Department of Energy Office of Science User Facility located at Lawrence Berkeley National Laboratory, operated under Contract No. DE-AC02-05CH11231. S.P.S.S. and L.C.G. acknowledge the use of the Opuntia, Sabine, and Carya Clusters provided by the Research Computing Data Core at the University of Houston. We thank Jimmy K Soeherman and Xinyu Li for the helpful discussion related to infrared spectroscopy. We also thank Keith and Amy Steva for their generous support of this project through their donor advised fund.

Keywords. Energy, Catalysis, Storage, Dynamics, Platinum, Condenser

Supporting Information. The supporting information is available free of charge online.

Device fabrication, characterization methods, microscopy, electronic characterization, temperature programmed desorption methods, infrared photography, device performance calculations, computational methods, and additional references.[96,97,98,99,100]

Notes. The authors declare no competing financial interest

ORCID. Tzia Ming Onn: 0000-0002-7523-0746, Sallye R. Gathmann: 0000-0002-1001-6650, Silu Guo: 0000-0001-9930-6242, Surya Pratap S. Solanki: 0000-0003-1921-0983, Amber Walton: 0000-0003-0600-1613, Benjamin J. Page: 0000-0002-9114-555X, Geoffrey Rojas: 0000-0002-4458-9844, Matthew Neurock: 0000-0003-1458-7837, Lars C. Grabow: 0000-0002-7766-8856, K. Andre Mkhoyan: 0000-0003-3568-5452, Omar A. Abdelrahman: 0000-0001-6023-857X, C. Daniel Frisbie: 0000-0002-4735-2228, Paul J. Dauenhauer: 0000-0001-5810-1953

References.

(1) Boudart, M. Heterogeneous Catalysis by Metals. *J. Mol. Catal.* **1985**, *30* (1–2), 27–38. https://doi.org/10.1016/0304-5102(85)80014-6.

(2) Nørskov, J. K.; Bligaard, T.; Hvolbæk, B.; Abild-Pedersen, F.; Chorkendorff, I.; Christensen, C. H. The Nature of the Active Site in Heterogeneous Metal Catalysis. *Chem. Soc. Rev.* **2008**, *37* (10), 2163–2171. https://doi.org/10.1039/b800260f.

(3) Harris, P. J. F. Growth and Structure of Supported Metal Catalyst Particles. *Int. Mater. Rev.* **1995**, *40* (3), 97–115. https://doi.org/10.1179/imr.1995.40.3.97.

(4) Mitchell, S.; Pérez-Ramírez, J. Atomically Precise Control in the Design of Low-Nuclearity Supported Metal Catalysts. *Nat. Rev. Mater.* **2021**, *6* (11), 969–985. https://doi.org/10.1038/s41578-021-00360-6.

(5) Zhang, L.; Zhou, M.; Wang, A.; Zhang, T. Selective Hydrogenation over Supported Metal Catalysts: From Nanoparticles to Single Atoms. *Chem. Rev.* **2020**, *120* (2), 683–733. https://doi.org/10.1021/acs.chemrev.9b002

30.
(6) Hansgen, D. A.; Vlachos, D. G.; Chen, J. G. Using First Principles to Predict Bimetallic Catalysts for the Ammonia Decomposition Reaction. *Nat. Chem.* **2010**, *2* (6), 484–489. https://doi.org/10.1038/nchem.626.
(7) Hansgen, D. A.; Vlachos, D. G.; Chen, J. G. Ammonia Decomposition Activity on Monolayer Ni Supported on Ru, Pt and WC Substrates. *Surf. Sci.* **2011**, *605* (23–24), 2055–2060. https://doi.org/10.1016/j.susc.2011.08.004.
(8) Diao, W.; Digiulio, C. D.; Schaal, M. T.; Ma, S.; Monnier, J. R. An Investigation on the Role of Re as a Promoter in Ag-Cs-Re/α-Al2O3 High-Selectivity, Ethylene Epoxidation Catalysts. *J. Catal.* **2015**, *322*, 14–23. https://doi.org/10.1016/j.jcat.2014.11.007.
(9) Chen, B. W. J.; Wang, B.; Sullivan, M. B.; Borgna, A.; Zhang, J. Unraveling the Synergistic Effect of Re and Cs Promoters on Ethylene Epoxidation over Silver Catalysts with Machine Learning-Accelerated First-Principles Simulations. *ACS Catal.* **2022**, *12* (4), 2540–2551. https://doi.org/10.1021/acscatal.1c05419.
(10) van Deelen, T. W.; Hernández Mejía, C.; de Jong, K. P. Control of Metal-Support Interactions in Heterogeneous Catalysts to Enhance Activity and Selectivity. *Nat. Catal.* **2019**, *2* (11), 955–970. https://doi.org/10.1038/s41929-019-0364-x.
(11) Fujiwara, K.; Okuyama, K.; Pratsinis, S. E. Metal-Support Interactions in Catalysts for Environmental Remediation. *Environ. Sci. Nano* **2017**, *4* (11), 2076–2092. https://doi.org/10.1039/c7en00678k.
(12) Gawande, M. B.; Goswami, A.; Asefa, T.; Guo, H.; Biradar, A. V.; Peng, D. L.; Zboril, R.; Varma, R. S. Core-Shell Nanoparticles: Synthesis and Applications in Catalysis and Electrocatalysis. *Chem. Soc. Rev.* **2015**, *44* (21), 7540–7590. https://doi.org/10.1039/c5cs00343a.
(13) Das, S.; Pérez-Ramírez, J.; Gong, J.; Dewangan, N.; Hidajat, K.; Gates, B. C.; Kawi, S. Core-Shell Structured Catalysts for Thermocatalytic, Photocatalytic, and Electrocatalytic Conversion of CO2. *Chem. Soc. Rev.* **2020**, *49* (10), 2937–3004. https://doi.org/10.1039/c9cs00713j.
(14) Yang, Y.; Wei, M. Intermetallic Compound Catalysts: Synthetic Scheme, Structure Characterization and Catalytic Application. *J. Mater. Chem. A* **2020**, *8* (5), 2207–2221. https://doi.org/10.1039/c9ta09448b.
(15) Marakatti, V. S.; Peter, S. C. Synthetically Tuned Electronic and Geometrical Properties of Intermetallic Compounds as Effective Heterogeneous Catalysts. *Prog. Solid State Chem.* **2018**, *52*, 1–30. https://doi.org/10.1016/j.progsolidstchem.2018.09.001.
(16) T., H. R.; Georgios, G.; Romain, R.; Julia, S.; Jordan, F.; Yicheng, W.; Angelos, M.; Prashant, D.; Phillip, C.; Maria, F.-S.; Michail, S.; H., S. E. C. First-Principles Design of a Single-Atom–Alloy Propane Dehydrogenation Catalyst. *Science (80-.).* **2021**, *372* (6549), 1444–1447. https://doi.org/10.1126/science.abg8389.
(17) Hannagan, R. T.; Giannakakis, G.; Flytzani-Stephanopoulos, M.; Sykes, E. C. H. Single-Atom Alloy Catalysis. *Chem. Rev.* **2020**, *120* (21), 12044–12088. https://doi.org/10.1021/acs.chemrev.0c00078.
(18) Vogt, C.; Weckhuysen, B. M. The Concept of Active Site in Heterogeneous Catalysis. *Nat. Rev. Chem.* **2022**, *6* (2), 89–111. https://doi.org/10.1038/s41570-021-00340-y.
(19) Shetty, M.; Walton, A.; Gathmann, S. R.; Ardagh, M. A.; Gopeesingh, J.; Resasco, J.; Birol, T.; Zhang, Q.; Tsapatsis, M.; Vlachos, D. G.; Christopher, P.; Frisbie, C. D.; Abdelrahman, O. A.; Dauenhauer, P. J. The Catalytic Mechanics of Dynamic Surfaces: Stimulating Methods for Promoting Catalytic Resonance. *ACS Catal.* **2020**, 12666–12695. https://doi.org/10.1021/acscatal.0c03336.
(20) Dauenhauer, P. J.; Shetty, M.; Ardagh, M. A.; Pang, Y.; Abdelrahman, O. A. Electric-Field-Assisted Modulation of Surface Thermochemistry. *ACS Catal.* **2020**, *10* (21), 12867–12880. https://doi.org/10.1021/acscatal.0c02124.
(21) Onn, T. M.; Gathmann, S. R.; Wang, Y.;

Patel, R.; Guo, S.; Chen, H.; Soeherman, J. K.; Christopher, P.; Rojas, G.; Mkhoyan, K. A.; Neurock, M.; Abdelrahman, O. A.; Frisbie, C. D.; Dauenhauer, P. J. Alumina Graphene Catalytic Condenser for Programmable Solid Acids. *JACS Au* **2022**. https://doi.org/10.1021/jacsau.2c00114.

(22) Shigeishi, R. A.; King, D. A. Chemisorption of Carbon Monoxide on Platinum {111}: Reflection-Absorption Infrared Spectroscopy. *Surf. Sci.* **1976**, *58* (2), 379–396. https://doi.org/10.1016/0039-6028(76)90477-5.

(23) Horn, R.; Degenstein, N. J.; Williams, K. A.; Schmidt, L. D. Spatial and Temporal Profiles in Millisecond Partial Oxidation Processes. *Catal. Letters* **2006**, *110* (3), 169–178. https://doi.org/10.1007/s10562-006-0117-8.

(24) Cortright, R. D.; Davda, R. R.; Dumesic, J. A. Hydrogen from Catalytic Reforming of Biomass-Derived Hydrocarbons in Liquid Water. *Nature* **2002**, *418* (6901), 964–967. https://doi.org/10.1038/nature01009.

(25) Bodke, A. S.; Henning, D.; Schmidt, L. D.; Bharadwaj, S. S.; Maj, J. J.; Siddall, J. Oxidative Dehydrogenation of Ethane at Millisecond Contact Times: Effect of H2 Addition. *J. Catal.* **2000**, *191* (1), 62–74. https://doi.org/https://doi.org/10.1006/jcat.1999.2802.

(26) Vajda, S.; Pellin, M. J.; Greeley, J. P.; Marshall, C. L.; Curtiss, L. A.; Ballentine, G. A.; Elam, J. W.; Catillon-Mucherie, S.; Redfern, P. C.; Mehmood, F.; Zapol, P. Subnanometre Platinum Clusters as Highly Active and Selective Catalysts for the Oxidative Dehydrogenation of Propane. *Nat. Mater.* **2009**, *8* (3), 213–216. https://doi.org/10.1038/nmat2384.

(27) Bratlie, K. M.; Lee, H.; Komvopoulos, K.; Yang, P.; Somorjai, G. A. Platinum Nanoparticle Shape Effects on Benzene Hydrogenation Selectivity. *Nano Lett.* **2007**, *7* (10), 3097–3101. https://doi.org/10.1021/nl0716000.

(28) Adzic, R. R.; Zhang, J.; Sasaki, K.; Vukmirovic, M. B.; Shao, M.; Wang, J. X.; Nilekar, A. U.; Mavrikakis, M.; Valerio, J. A.; Uribe, F. Platinum Monolayer Fuel Cell Electrocatalysts. *Top. Catal.* **2007**, *46* (3), 249–262. https://doi.org/10.1007/s11244-007-9003-x.

(29) Morozan, A.; Jousselme, B.; Palacin, S. Low-Platinum and Platinum-Free Catalysts for the Oxygen Reduction Reaction at Fuel Cell Cathodes. *Energy Environ. Sci.* **2011**, *4* (4), 1238–1254. https://doi.org/10.1039/c0ee00601g.

(30) Berlowitz, P. J.; Peden, C. H. F.; Goodman, D. W. Kinetics of Carbon Monoxide Oxidation on Single-Crystal Palladium, Platinum, and Iridium. *J. Phys. Chem.* **1988**, *92* (18), 5213–5221. https://doi.org/10.1021/j100329a030.

(31) Lee, I.; Zaera, F. Chiral Templating of Surfaces: Adsorption of (S)-2-Methylbutanoic Acid on Pt(111) Single-Crystal Surfaces. *J. Am. Chem. Soc.* **2006**, *128* (27), 8890–8898. https://doi.org/10.1021/ja061654w.

(32) Resasco, J.; Dai, S.; Graham, G.; Pan, X.; Christopher, P. Combining In-Situ Transmission Electron Microscopy and Infrared Spectroscopy for Understanding Dynamic and Atomic-Scale Features of Supported Metal Catalysts. *J. Phys. Chem. C* **2018**, *122* (44), 25143–25157. https://doi.org/10.1021/acs.jpcc.8b03959.

(33) Yang, T. T.; Tan, T. L.; Saidi, W. A. High Activity toward the Hydrogen Evolution Reaction on the Edges of MoS2-Supported Platinum Nanoclusters Using Cluster Expansion and Electrochemical Modeling. *Chem. Mater.* **2020**, *32* (3), 1315–1321. https://doi.org/10.1021/acs.chemmater.9b05244.

(34) Greeley, J.; Stephens, I. E. L.; Bondarenko, A. S.; Johansson, T. P.; Hansen, H. A.; Jaramillo, T. F.; Rossmeisl, J.; Chorkendorff, I.; Nørskov, J. K. Alloys of Platinum and Early Transition Metals as Oxygen Reduction Electrocatalysts. *Nat. Chem.* **2009**, *1* (7), 552–556. https://doi.org/10.1038/nchem.367.

(35) Zhang, C.-X.; Gao, Y.-C.; Li, H.-W.; Wu, Y. Gold–Platinum Bimetallic Nanoclusters for Oxidase-like Catalysis. *ACS Appl. Nano Mater.* **2020**, *3* (9), 9318–9328. https://doi.org/10.1021/acsanm.0c01965.

(36) DeRita, L.; Dai, S.; Lopez-Zepeda, K.; Pham, N.; Graham, G. W.; Pan, X.;

Christopher, P. Catalyst Architecture for Stable Single Atom Dispersion Enables Site-Specific Spectroscopic and Reactivity Measurements of CO Adsorbed to Pt Atoms, Oxidized Pt Clusters, and Metallic Pt Clusters on TiO2. *J. Am. Chem. Soc.* **2017**, *139* (40), 14150–14165. https://doi.org/10.1021/jacs.7b07093.

(37) Thang, H. V.; Pacchioni, G.; DeRita, L.; Christopher, P. Nature of Stable Single Atom Pt Catalysts Dispersed on Anatase TiO2. *J. Catal.* **2018**, *367*, 104–114. https://doi.org/https://doi.org/10.1016/j.jcat.2018.08.025.

(38) Blaschke, D.; Munnik, F.; Grenzer, J.; Rebohle, L.; Schmidt, H.; Zahn, P.; Gemming, S. A Correlation Study of Layer Growth Rate, Thickness Uniformity, Stoichiometry, and Hydrogen Impurity Level in HfO2 Thin Films Grown by ALD between 100°C and 350°C. *Appl. Surf. Sci.* **2020**, *506*. https://doi.org/10.1016/j.apsusc.2019.144188.

(39) Gierałtowska, S.; Sztenkiel, D.; Guziewicz, E.; Godlewski, M.; Łuka, G.; Witkowski, B. S.; Wachnicki, L.; Łusakowska, E.; Dietl, T.; Sawicki, M. Properties and Characterization of ALD Grown Dielectric Oxides for MIS Structures. *Acta Phys. Pol. A* **2011**, *119* (5), 692–695. https://doi.org/10.12693/APhysPolA.119.692.

(40) Suk, J. W.; Kitt, A.; Magnuson, C. W.; Hao, Y.; Ahmed, S.; An, J.; Swan, A. K.; Goldberg, B. B.; Ruoff, R. S. Transfer of CVD-Grown Monolayer Graphene onto Arbitrary Substrates. *ACS Nano* **2011**, *5* (9), 6916–6924. https://doi.org/10.1021/nn201207c.

(41) Reina, A.; Son, H.; Jiao, L.; Fan, B.; Dresselhaus, M. S.; Liu, Z. F.; Kong, J. Transferring and Identification of Single- and Few-Layer Graphene on Arbitrary Substrates. *J. Phys. Chem. C* **2008**, *112* (46), 17741–17744. https://doi.org/10.1021/jp807380s.

(42) Kondo, T.; Izumi, K.; Watahiki, K.; Iwasaki, Y.; Suzuki, T.; Nakamura, J. Promoted Catalytic Activity of a Platinum Monolayer Cluster on Graphite. *J. Phys. Chem. C* **2008**, *112* (40), 15607–15610. https://doi.org/10.1021/jp8069833.

(43) Siburian, R.; Ali, A. M. M.; Sebayang, K.; Supeno, M.; Tarigan, K.; Simanjuntak, C.; Aritonang, S. P.; Hutagalung, F. The Loading Effect of Pt Clusters on Pt/Graphene Nano Sheets Catalysts. *Sci. Rep.* **2021**, *11* (1), 2532. https://doi.org/10.1038/s41598-020-80472-1.

(44) Jeong, S. J.; Gu, Y.; Heo, J.; Yang, J.; Lee, C. S.; Lee, M. H.; Lee, Y.; Kim, H.; Park, S.; Hwang, S. Thickness Scaling of Atomic-Layer-Deposited HfO2 Films and Their Application to Wafer-Scale Graphene Tunnelling Transistors. *Sci. Rep.* **2016**, *6*. https://doi.org/10.1038/srep20907.

(45) Jung, H. S.; Jang, J. H.; Cho, D. Y.; Jeon, S. H.; Kim, H. K.; Lee, S. Y.; Hwang, C. S. The Effects of Postdeposition Annealing on the Crystallization and Electrical Characteristics of HfO2 and ZrO2 Gate Dielectrics. *Electrochem. Solid-State Lett.* **2011**, *14* (5). https://doi.org/10.1149/1.3551460.

(46) Xie, Y.; Ma, Z.; Su, Y.; Liu, Y.; Liu, L.; Zhao, H.; Zhou, J.; Zhang, Z.; Li, J.; Xie, E. The Influence of Mixed Phases on Optical Properties of HfO2 Thin Films Prepared by Thermal Oxidation. *J. Mater. Res.* **2011**, *26* (1), 50–54. https://doi.org/10.1557/jmr.2010.61.

(47) He, G.; Liu, M.; Zhu, L. Q.; Chang, M.; Fang, Q.; Zhang, L. D. Effect of Postdeposition Annealing on the Thermal Stability and Structural Characteristics of Sputtered HfO2 Films on Si (1 0 0). *Surf. Sci.* **2005**, *576* (1–3), 67–75. https://doi.org/10.1016/j.susc.2004.11.042.

(48) Zhang, X. Y.; Hsu, C. H.; Lien, S. Y.; Wu, W. Y.; Ou, S. L.; Chen, S. Y.; Huang, W.; Zhu, W. Z.; Xiong, F. B.; Zhang, S. Temperature-Dependent HfO2/Si Interface Structural Evolution and Its Mechanism. *Nanoscale Res. Lett.* **2019**, *14*. https://doi.org/10.1186/s11671-019-2915-0.

(49) Holmberg, N.; Laasonen, K.; Peljo, P. Charge Distribution and Fermi Level in Bimetallic Nanoparticles. *Phys. Chem. Chem. Phys.* **2016**, *18* (4), 2924–2931.

https://doi.org/10.1039/c5cp07116j.
(50) Feibelman, P. J.; Hammer, B.; Nørskov, J. K.; Wagner, F.; Scheffler, M.; Stumpf, R.; Watwe, R.; Dumesic, J. The CO/Pt(111) Puzzle. *J. Phys. Chem. B* **2001**, *105* (18), 4018–4025. https://doi.org/10.1021/jp002302t.
(51) Grinberg, I.; Yourdshahyan, Y.; Rappe, A. M. CO on PT(111) Puzzle: A Possible Solution. *J. Chem. Phys.* **2002**, *117* (5), 2264–2270. https://doi.org/10.1063/1.1488596.
(52) Janthon, P.; Viñes, F.; Sirijaraensre, J.; Limtrakul, J.; Illas, F. Adding Pieces to the CO/Pt(111) Puzzle: The Role of Dispersion. *J. Phys. Chem. C* **2017**, *121* (7), 3970–3977. https://doi.org/10.1021/acs.jpcc.7b00365.
(53) Kalhara Gunasooriya, G. T. K.; Saeys, M. CO Adsorption Site Preference on Platinum: Charge Is the Essence. *ACS Catal.* **2018**, *8* (5), 3770–3774. https://doi.org/10.1021/acscatal.8b00214.
(54) Grabow, L. C.; Hvolbæk, B.; Nørskov, J. K. Understanding Trends in Catalytic Activity: The Effect of Adsorbate–Adsorbate Interactions for CO Oxidation Over Transition Metals. *Top. Catal.* **2010**, *53* (5), 298–310. https://doi.org/10.1007/s11244-010-9455-2.
(55) Gunasooriya, G. T. K. K.; Saeys, M. CO Adsorption on Pt(111): From Isolated Molecules to Ordered High-Coverage Structures. *ACS Catal.* **2018**, *8* (11), 10225–10233. https://doi.org/10.1021/acscatal.8b02371.
(56) McCabe, R. W.; Schmidt, L. D. Binding States of CO and H2 on Clean and Oxidized (111)Pt. *Surf. Sci.* **1977**, *65* (1), 189–209. https://doi.org/https://doi.org/10.1016/0039-6028(77)90301-6.
(57) Ertl, G.; Neumann, M.; Streit, K. M. Chemisorption of CO on the Pt(111) Surface. *Surf. Sci.* **1977**, *64* (2), 393–410. https://doi.org/https://doi.org/10.1016/0039-6028(77)90052-8.
(58) Allian, A. D.; Takanabe, K.; Fujdala, K. L.; Hao, X.; Truex, T. J.; Cai, J.; Buda, C.; Neurock, M.; Iglesia, E. Chemisorption of CO and Mechanism of CO Oxidation on Supported Platinum Nanoclusters. *J. Am. Chem. Soc.* **2011**, *133* (12), 4498–4517. https://doi.org/10.1021/ja110073u.
(59) Barteau, M. A.; Ko, E. I.; Madix, R. J. The Adsorption of CO, O2, and H2 on Pt(100)-(5×20). *Surf. Sci.* **1981**, *102* (1), 99–117. https://doi.org/https://doi.org/10.1016/0039-6028(81)90310-1.
(60) Park, Y. O.; Banholzer, W. F.; Masel, R. I. Adsorption and Interaction of CO and NO on Pt(410): I. TPD Studies. *Surf. Sci.* **1985**, *155* (1), 341–365. https://doi.org/https://doi.org/10.1016/0039-6028(85)90422-4.
(61) Siddiqui, H. R.; Guo, X.; Chorkendorff, I.; Yates, J. T. Co Adsorption Site Exchange between Step and Terrace Sites on Pt(112). *Surf. Sci.* **1987**, *191* (1), L813–L818. https://doi.org/https://doi.org/10.1016/S0039-6028(87)81043-9.
(62) Luo, J. S.; Tobin, R. G.; Lambert, D. K.; Fisher, G. B.; DiMaggio, C. L. CO Adsorption Site Occupation on Pt(335): A Quantitative Investigation Using TPD and EELS. *Surf. Sci.* **1992**, *274* (1), 53–62. https://doi.org/https://doi.org/10.1016/0039-6028(92)90099-R.
(63) Garrone, E.; Areán, C. O. Variable Temperature Infrared Spectroscopy: A Convenient Tool for Studying the Thermodynamics of Weak Solid–Gas Interactions. *Chem. Soc. Rev.* **2005**, *34* (10), 846–857. https://doi.org/10.1039/b407049f.
(64) Bonelli, B.; Areán, C. O.; Armandi, M.; Delgado, M. R.; Garrone, E. Variable-Temperature Infrared Spectroscopy Studies on the Thermodynamics of CO Adsorption on the Zeolite Ca-Y. *ChemPhysChem* **2008**, *9* (12), 1747–1751. https://doi.org/10.1002/cphc.200800238.
(65) Otero Areán, C.; Manoilova, O. V.; Turnes Palomino, G.; Rodríguez Delgado, M.; Tsyganenko, A. A.; Bonelli, B.; Garrone, E. Variable-Temperature Infrared Spectroscopy: An Access to Adsorption Thermodynamics of Weakly Interacting Systems. *Phys. Chem. Chem. Phys.* **2002**, *4* (23), 5713–5715. https://doi.org/10.1039/b209299a.

(66) Borchert, H.; Fenske, D.; Kolny-Olesiak, J.; Parisi, J.; Al-Shamery, K.; Bäumer, M. Ligand-Capped Pt Nanocrystals as Oxide-Supported Catalysts: FTIR Spectroscopic Investigations of the Adsorption and Oxidation of CO. *Angew. Chemie - Int. Ed.* **2007**, *46* (16), 2923–2926. https://doi.org/10.1002/anie.200604460.

(67) Lan, J.; Hutter, J.; Iannuzzi, M. First-Principles Simulations of an Aqueous CO/Pt(111) Interface. *J. Phys. Chem. C* **2018**, *122* (42), 24068–24076. https://doi.org/10.1021/acs.jpcc.8b05933.

(68) Ding, K.; Gulec, A.; Johnson, A. M.; Schweitzer, N. M.; Stucky, G. D.; Marks, L. D.; Stair, P. C. Identification of Active Sites in CO Oxidation and Water-Gas Shift over Supported Pt Catalysts. *Science (80-.).* **2015**, *350* (6257), 189–192. https://doi.org/10.1126/science.aac6368.

(69) NIST Webbook https://webbook.nist.gov/ (accessed Jul 30, 2022).

(70) An, Q.; Qian, J.; Nielsen, R. R.; Sementa, L.; Barcaro, G.; Negreiros, F. R.; Fortunelli, A.; Goddard III, W. A. The Quantum Mechanics Derived Atomistic Mechanism Underlying the Acceleration of Catalytic CO Oxidation on Pt(110) by Surface Acoustic Waves. *J. Mater. Chem. A* **2016**, *4* (31), 12036–12045. https://doi.org/10.1039/c6ta03669d.

(71) Gathmann, S. R.; Ardagh, M. A.; Dauenhauer, P. J. Catalytic Resonance Theory: Negative Dynamic Surfaces for Programmable Catalysts. *Chem Catal.* **2022**. https://doi.org/10.1016/j.checat.2021.12.006.

(72) Ardagh, M. A.; Abdelrahman, O. A.; Dauenhauer, P. J. Principles of Dynamic Heterogeneous Catalysis: Surface Resonance and Turnover Frequency Response. *ACS Catal.* **2019**, *9* (8), 6929–6937. https://doi.org/10.1021/acscatal.9b01606.

(73) Ardagh, M. A.; Birol, T.; Zhang, Q.; Abdelrahman, O. A.; Dauenhauer, P. J. Catalytic Resonance Theory: SuperVolcanoes, Catalytic Molecular Pumps, and Oscillatory Steady State. *Catal. Sci. Technol.* **2019**, *9* (18), 5058–5076. https://doi.org/10.1039/c9cy01543d.

(74) Dauenhauer, P. J.; Ardagh, M. A.; Shetty, M.; Kuznetsov, A.; Zhang, Q.; Christopher, P.; Vlachos, D. G.; Abdelrahman, O. A. Catalytic Resonance Theory: Parallel Reaction Pathway Control. *Chem. Sci.* **2020**, *11* (13), 3501–3510. https://doi.org/10.1039/c9sc06140a.

(75) Gopeesingh, J.; Ardagh, M. A.; Shetty, M.; Burke, S. T.; Dauenhauer, P. J.; Abdelrahman, O. A. Resonance-Promoted Formic Acid Oxidation via Dynamic Electrocatalytic Modulation. *ACS Catal.* **2020**, *10* (17), 9932–9942. https://doi.org/10.1021/acscatal.0c02201.

(76) R., W. G.; Shizhong, L.; J., D. P.; G., V. D. Catalytic Resonance of Ammonia Synthesis by Simulated Dynamic Ruthenium Crystal Strain. *Sci. Adv.* **2022**, *8* (4), eabl6576. https://doi.org/10.1126/sciadv.abl6576.

(77) Sun, S.; Zhang, G.; Gauquelin, N.; Chen, N.; Zhou, J.; Yang, S.; Chen, W.; Meng, X.; Geng, D.; Banis, M. N.; Li, R.; Ye, S.; Knights, S.; Botton, G. A.; Sham, T.-K.; Sun, X. Single-Atom Catalysis Using Pt/Graphene Achieved through Atomic Layer Deposition. *Sci. Rep.* **2013**, *3* (1), 1775. https://doi.org/10.1038/srep01775.

(78) Cheng, N.; Stambula, S.; Wang, D.; Banis, M. N.; Liu, J.; Riese, A.; Xiao, B.; Li, R.; Sham, T.-K.; Liu, L.-M.; Botton, G. A.; Sun, X. Platinum Single-Atom and Cluster Catalysis of the Hydrogen Evolution Reaction. *Nat. Commun.* **2016**, *7* (1), 13638. https://doi.org/10.1038/ncomms13638.

(79) Zhifei, Y.; Dooyong, L.; Jin, Y.; Judith, G.; Tien-Lin, L.; D., J. R.; A., C. S.; Bharat, J. Epitaxial SrTiO3 Films with Dielectric Constants Exceeding 25,000. *Proc. Natl. Acad. Sci.* **2022**, *119* (23), e2202189119. https://doi.org/10.1073/pnas.2202189119.

(80) Buscaglia, V.; Randall, C. A. Size and Scaling Effects in Barium Titanate. An Overview. *J. Eur. Ceram. Soc.* **2020**, *40* (11), 3744–3758. https://doi.org/https://doi.org/10.1016/j.jeurceramsoc.2020.01.021.

(81) Joubert, D. From Ultrasoft Pseudopotentials to the Projector

Augmented-Wave Method. *Phys. Rev. B - Condens. Matter Mater. Phys.* **1999**, *59* (3), 1758–1775. https://doi.org/10.1103/PhysRevB.59.1758.

(82) Kresse, G.; Furthmüller, J. Efficiency of Ab-Initio Total Energy Calculations for Metals and Semiconductors Using a Plane-Wave Basis Set. *Comput. Mater. Sci.* **1996**, *6* (1), 15–50. https://doi.org/10.1016/0927-0256(96)00008-0.

(83) Kresse, G.; Furthmüller, J. Efficient Iterative Schemes for Ab Initio Total-Energy Calculations Using a Plane-Wave Basis Set. *Phys. Rev. B - Condens. Matter Mater. Phys.* **1996**, *54* (16), 11169–11186. https://doi.org/10.1103/PhysRevB.54.11169.

(84) Kresse, G.; Hafner, J. Ab Initio Molecular Dynamics for Liquid Metals. *Phys. Rev. B* **1993**, *47* (1), 558–561. https://doi.org/10.1103/PhysRevB.47.558.

(85) Hohenberg, P.; Kohn, W. Inhomogeneous Electron Gas. *Phys. Rev.* **1964**, *136* (3B). https://doi.org/10.1103/PhysRev.136.B864.

(86) Kohn, W.; Sham, L. J. Self-Consistent Equations Including Exchange and Correlation Effects. *Phys. Rev.* **1965**, *140* (4A). https://doi.org/10.1103/PhysRev.140.A1133.

(87) Hjorth Larsen, A.; JØrgen Mortensen, J.; Blomqvist, J.; Castelli, I. E.; Christensen, R.; Dułak, M.; Friis, J.; Groves, M. N.; Hammer, B.; Hargus, C.; Hermes, E. D.; Jennings, P. C.; Bjerre Jensen, P.; Kermode, J.; Kitchin, J. R.; Leonhard Kolsbjerg, E.; Kubal, J.; Kaasbjerg, K.; Lysgaard, S.; Bergmann Maronsson, J.; Maxson, T.; Olsen, T.; Pastewka, L.; Peterson, A.; Rostgaard, C.; SchiØtz, J.; Schütt, O.; Strange, M.; Thygesen, K. S.; Vegge, T.; Vilhelmsen, L.; Walter, M.; Zeng, Z.; Jacobsen, K. W. The Atomic Simulation Environment - A Python Library for Working with Atoms. *J. Phys. Condens. Matter* **2017**, *29* (27). https://doi.org/10.1088/1361-648X/aa680e.

(88) Perdew, J. P.; Burke, K.; Ernzerhof, M. Generalized Gradient Approximation Made Simple. *Phys. Rev. Lett.* **1996**, *77* (18), 3865–3868. https://doi.org/10.1103/PhysRevLett.77.3865.

(89) Ernzerhof, M.; Scuseria, G. E. Assessment of the Perdew-Burke-Ernzerhof Exchange-Correlation Functional. *J. Chem. Phys.* **1999**, *110* (11), 5029–5036. https://doi.org/10.1063/1.478401.

(90) Blöchl, P. E. Projector Augmented-Wave Method. *Phys. Rev. B* **1994**, *50* (24), 17953–17979. https://doi.org/10.1103/PhysRevB.50.17953.

(91) Yu, M.; Trinkle, D. R. Accurate and Efficient Algorithm for Bader Charge Integration. *J. Chem. Phys.* **2011**, *134* (6). https://doi.org/10.1063/1.3553716.

(92) Tang, W.; Sanville, E.; Henkelman, G. A Grid-Based Bader Analysis Algorithm without Lattice Bias. *J. Phys. Condens. Matter* **2009**, *21* (8). https://doi.org/10.1088/0953-8984/21/8/084204.

(93) Henkelman, G.; Arnaldsson, A.; Jónsson, H. A Fast and Robust Algorithm for Bader Decomposition of Charge Density. *Comput. Mater. Sci.* **2006**, *36* (3), 354–360. https://doi.org/10.1016/j.commatsci.2005.04.010.

(94) Mathew, K.; Kolluru, V. S. C.; Mula, S.; Steinmann, S. N.; Hennig, R. G. Implicit Self-Consistent Electrolyte Model in Plane-Wave Density-Functional Theory. *J. Chem. Phys.* **2019**, *151* (23). https://doi.org/10.1063/1.5132354.

(95) Mathew, K.; Sundararaman, R.; Letchworth-Weaver, K.; Arias, T. A.; Hennig, R. G. Implicit Solvation Model for Density-Functional Study of Nanocrystal Surfaces and Reaction Pathways. *J. Chem. Phys.* **2014**, *140* (8). https://doi.org/10.1063/1.4865107.

(96) Wang, Y.; Udyavara, S.; Neurock, M.; Daniel Frisbie, C. Field Effect Modulation of Electrocatalytic Hydrogen Evolution at Back-Gated Two-Dimensional MoS2 Electrodes. *Nano Lett.* **2019**, *19* (9), 6118–6123. https://doi.org/10.1021/acs.nanolett.9b02079.

(97) Redhead, P. A. Thermal Desorption of Gases. *Vacuum* **1962**, *12* (4), 203–211.

https://doi.org/10.1016/0042-207X(62)90978-8.
(98) McCabe, R. W.; Schmidt, L. D. Adsorption of H2 and CO on Clean and Oxidized (110) Pt. *Surf. Sci.* **1976**, *60* (1), 85–98. https://doi.org/10.1016/0039-6028(76)90008-X.
(99) Savara, A. Standard States for Adsorption on Solid Surfaces: 2D Gases, Surface Liquids, and Langmuir Adsorbates. *J. Phys. Chem. C* **2013**, *117* (30), 15710–15715. https://doi.org/10.1021/jp404398z.
(100) Johnson, R. D. Computational Chemisty Comparison and Benchmark (CCCBDB) Database https://cccbdb.nist.gov/ (accessed Aug 6, 2022). https://doi.org/10.18434/T47C7Z.